

On the potential of ICOS atmospheric CO₂ measurement network for the estimation of the biogenic CO₂ budget of Europe

N. Kadygrov¹, G. Broquet¹, F. Chevallier¹, L. Rivier¹, C. Gerbig² and P. Ciais¹

¹ Laboratoire des Sciences du Climat et de l'Environnement, CEA-CNRS-UVSQ, 91191, Gif sur Yvette Cedex, France

² Max Planck Institute for Biogeochemistry, Jena, Germany

Correspondence to: N. Kadygrov (kadygrov@gmail.com)

Abstract

We present a performance assessment of the European Integrated Carbon Observing System (ICOS) atmospheric network for constraining European biogenic CO₂ fluxes (hereafter Net Ecosystem Exchange, NEE). The performance of the network is assessed in terms of uncertainty in the fluxes using a state-of-the-art mesoscale variational atmospheric inversion system assimilating hourly averages of atmospheric data to solve for NEE at 6 hour and 0.5° resolution. The performance of the ICOS atmospheric network is also assessed in terms of uncertainty reduction compared to typical uncertainties in the flux estimates from ecosystem models that are used as prior information by the inversion. The uncertainty in inverted fluxes is computed for two typical periods representative of summer and winter conditions in July and in December 2007, respectively. These computations are based on a Observing System Simulation Experiment framework. We analyze the uncertainty in two-week mean NEE as a function of the spatial scale, with a focus on the model native grid scale (0.5°), the country scale and the European scale (including western Russia and Turkey). Several network configurations, going from 23 to 66 sites, and different configurations of the prior uncertainties and atmospheric model transport errors are tested in order to assess and compare the improvements that can be expected in the future from 1) the extension of the network, 2) improved prior information or 3) improved transport models. Assimilating data from 23 sites (a network comparable to present day capability) with the estimate of errors from the present prior information and transport models, the uncertainty reduction on two-week mean NEE should range between 20% and 50% for 0.5° resolution grid cells in the best sampled area encompassing eastern France and western Germany. At the European scale, the prior uncertainty in two-week mean NEE is reduced by 50% (66%), down to ~ 43 TgCmonth⁻¹ (26 TgCmonth⁻¹) in July (December). Using a larger network of 66 stations, the prior uncertainty of NEE is reduced by the inversion by 64% (down to ~33 TgC month⁻¹) in July and by 79% (down to ~15 TgC month⁻¹) in December. When the results are integrated over the well-observed western European domain, the uncertainty reduction

shows no seasonal contrast. The effect of decreasing the correlation length of the prior uncertainty, or of reducing the transport model errors compared to their present configuration (when conducting real-data inversion cases) can be larger than that of the extension of the measurement network in areas where the 23 stations observation network is the densest. We show that with a configuration of the ICOS atmospheric network containing 66 sites that can be expected on the long-term, the uncertainties in two-week mean NEE will be reduced by up to 50-80 % for countries like Finland, Germany, France and Spain, which could bring a significant improvement of (and at least a high complementarity to) our knowledge about NEE derived from biomass and soil carbon inventories at multi annual scales.

1 Introduction

Accurate information about the terrestrial biogenic CO₂ fluxes (hereafter Net Ecosystem Exchange - NEE) is needed at the regional scale to understand the drivers of the carbon cycle. Accounting for the natural fluxes in political agreements regarding the reduction of the CO₂ emissions requires their accurate quantification over administrative areas, and in particular over countries and smaller regional scales at which land management decisions can be implemented. Atmospheric inversions, which exploit atmospheric CO₂ mole fraction measurements to infer information about surface CO₂ fluxes (Enting, 2002) are expected to deliver robust and objective quantification of NEE at high temporal and spatial resolution over continuous areas and time periods. Global atmospheric inversions have been widely used to document natural carbon sources and sinks (Gurney et al., 2002, Rodenbeck et al., 2003), although the spread of different studies, and thus, likely the uncertainty (which is confirmed when it is diagnosed by the inversion studies), remain large at the one month and continental scale (Peylin et al., 2013). Such large uncertainties are mainly due to the lack of observations over the continents or to the limited ability of global systems to account for dense observation networks in addition to errors in large-

scale atmospheric transport models. However, with an increasing number of continuous atmospheric CO₂ observations, primarily in North America and Europe, and with the development of regional inversion systems using high resolution mesoscale atmospheric transport models and solving for NEE at typical resolutions of 10 to 50 km (Lauvaux et al., 2008, 2012, Schuh et al., 2010, Broquet et al., 2011, Meesters et al., 2012), there is an increasing ability to constrain NEE at continental to regional scales.

This paper aims at studying the skill of a regional inversion in Europe, which is equipped with a relatively large number of ground-based atmospheric measurement stations, for estimating NEE at the continental and country scales, down to 0.5° resolution (which is the resolution of the transport model used in the inversion system). It also aims at assessing and comparing the benefits from the measurement network extensions and from future improvement in the inversion system. Such improvement can be anticipated either due to better atmospheric transport models or to the use of better flux estimates as the prior information that gets updated by the inversion based on the assimilation of atmospheric measurements.

Europe is a difficult application area for atmospheric inversion because of the very heterogeneous distribution of vegetation types, land use, and agricultural and industrial activities inside a relatively small domain, and, consequently, because of the need for solving for fluxes at high resolution. Furthermore, its complex terrain also requires a high resolution of the topography when modeling the atmospheric transport (Ahmadov et al., 2009). However, the Integrated Carbon Observing System (ICOS) infrastructure is setting up a dense network of standardized, long-term, continuous and high precision atmospheric and flux measurements in Europe, with the aim of understanding the European carbon balance and monitoring the effectiveness of Greenhouse Gas (GHG) mitigation activities (<http://www.icos-infrastructure.eu/>). The atmospheric network is expected to increase from an initial configuration of around 23 stations (most existing today, hereafter ICOS23) up to around 60 stations in the

near future (see ICOS Stakeholder handbook 2013 at https://icos-atc.lsce.ipsl.fr/?q=doc_public).

In this context, the developers of the ICOS atmospheric network have encouraged network assessment studies such as the one conducted in this paper.

Several inversion studies have focused on the estimate of European NEE based on actual measurements from the CarboEurope-IP atmospheric stations, most of which are planning to join the ICOS atmospheric network (Peters et al., 2010, Broquet et al., 2011). Broquet et al. (2013) have demonstrated, based on comparisons to independent flux tower measurements, that there is a high confidence in the Bayesian estimate of the European NEE and of its uncertainty at the 1-month and continental scale based on their variational system which uses the CHIMERE mesoscale transport model run at 0.5° resolution. Indeed, the distributions of the misfits between 1 month and continental scale averages of the flux measurements and of the NEE estimates sampled at the flux measurement locations revealed to be unbiased and consistent with the estimate of the uncertainties from the inversion system. This gives confidence in the configuration of this system, described in Broquet et al. (2011, 2013), and in the underlying assumptions (e.g. on the unbiased and Gaussian distribution of the uncertainties, or regarding the weak impact of the uncertainties in the CO₂ modeling domain boundary conditions at the edges of Europe, or in the CO₂ fossil fuel emissions) for the estimation of the performance of the ICOS network.

Therefore, here, we apply the system of Broquet et al. (2011, 2013) to assess the potential of the near term and of realistic future configurations of the ICOS continuous measurements of CO₂ dry air mole fraction to improve NEE estimates at mesoscale across Europe. This assessment is based on a quantitative evaluation of the uncertainties in the inverted fluxes (also called posterior uncertainties) which are compared to the uncertainties in the prior information on NEE used by the inversion system. The Bayesian statistical framework chosen here provides estimates of the posterior uncertainties as a function of the prior uncertainties, of the atmospheric transport and of

the combination of statistical errors which are not controlled by the update of the prior NEE by the inversion (like the measurement errors and the atmospheric transport errors). Even though the prior uncertainty can potentially depend on the value of the prior NEE, the actual values of the prior NEE or of the measurement data to be assimilated are not formally involved in the estimation of the posterior uncertainty due to the linearity of the atmospheric transport of CO₂. Therefore, the posterior uncertainty can be derived for hypothetical observation networks or for hypothetical uncertainties in the prior information or from the atmospheric transport model (i.e., for hypothetical improvements in the prior information or in the atmospheric transport model) using an Observing System Simulation Experiment (OSSE) framework, in which the results do not depend on a simulated truth. Due to the dimension of the problem, uncertainties are not derived analytically in this study and we use a Monte Carlo ensemble approach. Using synthetic data in an OSSE framework has been a common way to assess the utility of new GHG observing systems for the monitoring of the GHG sources and sinks at large scales based on global inversion systems with coarse resolution transport models (e.g., Rayner et al., 1996, Houweling et al., 2004, Chevallier et al., 2007, Kadyrov et al., 2009, Hungershofer et al., 2010). This approach now plays a critical role in the recent emergence of regional inversion systems supporting strategies for the deployment of regional observation networks and assessing the potential of regional inversion for assessing the GHG fluxes at a relatively high resolution (Tolk et al., 2011, Ziehn et al., 2014). Such a use of OSSEs today is not specific to the GHG inversion community. OSSEs are increasingly used by the air quality community (e.g., Edwards et al., 2009, Timmermans et al. 2009a, b, Claeysman et al., 2011) and they are still extensively used by the meteorological community (e.g., Masutani et al., 2010, Riishojgaard et al., 2012, Errico et al., 2013, see also https://www.gmes-atmosphere.eu/events/osse_workshop/). In these fields, twin experiments are often used to derive a single realization of the uncertainties (Masutani et al., 2010) while our Monte Carlo approach explores the uncertainty space much more extensively. Further, in common (linear) CO₂ atmospheric inversions, since the results are independent of the

synthetic “true” data used for the OSSE, any simulation can be used to build this truth, while, when using fraternal twin experiments with nonlinear models in other application fields of data assimilation, it is critical to ensure that the truth is realistic enough (Halliwell et al., 2014). Still, the reliability of the OSSEs in CO₂ atmospheric inversion critically depends on the realism of their input error statistics since their configuration in the inversion system is perfectly consistent with the sampling of synthetic errors that are used in these experiments. In this study, our confidence in the realism of the statistical modeling approach and of the input error statistics, and thus in the inversion set-up, is based on the statistical modeling studies of Chevallier et al. (2012) and Broquet et al. (2013) that were themselves based on real data.

The manuscript first documents the potential for constraining NEE, through the use of a state-of-the-art (i.e. which solves the NEE at high spatial and temporal resolution, and which has been submitted to a high level of evaluation) variational atmospheric inversion system, and of the ICOS23 network containing existing sites and other stations that could be installed on tall towers over Europe in the coming years. We also consider two longer-term ICOS configurations with 50 (hereafter ICOS50) and 66 stations (hereafter ICOS66), respectively. For the time domain, we consider results for NEE aggregated at the two-week scale, for two different periods of the year (in July and in December). Shorter aggregation scales, like the day, result in a significant dependency of NEE to specific synoptic events. Longer scales imply computing resources that are beyond the scope of this study with this high-resolution inversion system. We pay special attention to the analysis of the results at different spatial scales, from the native transport model grid scale of about 50x50 km² up to the national scale that is the most relevant for supporting environmental policy, and the full European domain considered in this study (which extends to western Russia and Turkey). We also present the sensitivity of our results to parameters characterizing the future developments of the mesoscale inversion systems: the reduction of the transport model errors or of the prior flux errors.

The paper is organized as follows. Section 2 describes the mesoscale inversion experimental framework focusing on the Monte Carlo estimate of uncertainties. Section 3 analyses the scores of posterior uncertainties and the uncertainty reduction compared to the prior uncertainties in order to assess the potential of the near term framework and the one of future improvements of the network or of the inversion set-up. The last section synthesizes the results and discusses them.

2 Materials and Methods

2.1 The configurations of the ICOS atmospheric observation network

We consider three successive phases of deployment of the ICOS atmospheric network. The initial state ICOS23 configuration includes 23 sites among which there are eight tall towers. This minimum network configuration is based on existing stations, most of them being operational in the CarboEurope-IP FP6 project. The ICOS network is expected to further expand during the next 5 years (according to the country declarations at the ICOS Interim Stakeholder Council and to the ICOS European Research Infrastructure Consortium 5 year financial plan). Using possible locations for the future stations, including sites that have already been discussed with the ICOS consortium during the ICOS preparatory phase FP7 project (European Union's Seventh Research Framework Programme, grant agreement No. 211574), we derived two plausible ICOS configurations: ICOS50 with 50 sites including 24 tall towers and ICOS66 with 66 sites including 33 tall towers.

The locations and details on the sites of the three configurations are summarized in Table A1 and in Fig. 1. Here, the existing and future ICOS CO₂ observations are assumed to comply with the World Meteorological Organization (WMO) accuracy targets of 0.1 parts per million (ppm) measurement precision (WMO, 1981, Francey, 1998) so that the measurement error is negligible

in comparison to the other type of errors that have to be accounted for in the inversion framework such as the model transport and representation errors (see their typical estimate in Sect. 2.2.2).

2.2 Mesoscale inversion system

2.2.1 Method

The estimate of uncertainties related to the different ICOS networks is based on an ensemble of inversions with the variational inversion system of Broquet et al. (2011), assimilating synthetic hourly averages of the atmospheric CO₂ data from these networks (over restricted time windows everyday depending on the type of sites that are considered, see Sect. 2.2.2.). A regional atmospheric transport model (see its description below) is used to estimate the relationship between the CO₂ fluxes and the CO₂ mixing ratios. The inversion system solves for 6-hour mean NEE on each grid point of the 0.5° by 0.5° resolution grid used for the transport modeling. It also solves for 6-hour mean ocean fluxes at 0.5° spatial resolution in order to account for errors from air-sea fluxes when mapping fluxes into hourly mean mixing ratios. However, analyzing the uncertainty reduction for ocean fluxes is out of the scope of this paper. Peylin et al. (2011) indicate that uncertainties in anthropogenic fluxes yield errors when simulating CO₂ mixing ratios at ICOS stations that are smaller than atmospheric model errors. Furthermore, the relative uncertainty in anthropogenic emissions is smaller than that in NEE, while on short timescales, the anthropogenic signal is generally smaller than the signature of the NEE at sites that are not very close (typically at less than 40km) to strong anthropogenic sources such as cities (see the analysis for the Trainou ICOS station near Orléans, in France by Bréon et al. 2015). Relying on such indications, we assume that the errors due to uncertainties in anthropogenic emissions are negligible compared to errors from NEE and atmospheric model errors. This is a fair assumption as long as most ICOS stations are relatively far from large urban areas, which should be the case

since the ICOS atmospheric station specification document (https://icos-atc.lsce.ipsl.fr/?q=doc_public) recommends that the measurements sites are located at more than 40km from the strong anthropogenic sources (such as the cities). Zhang et al. (2015) yield conclusions from their transport experiments at 1° resolution which contradict this assumption and this clearly raises an open debate. However, the evaluation of the inversion configuration from Broquet et al. (2013) supports our use of this assumption for our study. Therefore, in order to simulate the full amount of CO₂ in the atmosphere, the inversion uses a fixed estimate of the fossil fuel emissions (see below) without attempting at correcting it nor at accounting for uncertainties in these fluxes. The inversion also uses a fixed estimate of the CO₂ boundary conditions at the lateral and top boundaries of the regional modeling domain without attempting at correcting it or at accounting for uncertainties in these conditions. This follows the protocol from Broquet et al. (2011) which assumed that the error from the boundary conditions for the European domain is mainly a bias and which corrects for such a bias in a preliminary step that is independent to the subsequent application of the inversion. Again such an assumption is supported by the evaluation of the inversion configuration by Broquet et al. (2013). The relatively weak impact of uncertainties in the boundary conditions in Europe (while studies in other regions such as that of Gockede et al. (2010) indicate a high influence of such uncertainties) can be explained by the fact that the spatial scale of the incoming CO₂ patterns at the ICOS sites from remote sources and sinks outside the European domain boundaries is relatively large due to the atmospheric diffusion (especially under west wind conditions, when the air comes from the Atlantic ocean) compared to the typical distances between the ICOS sites. In principle, the inversion mainly exploits the smaller scale signal of the gradients between the sites to constrain the NEE, and it is thus weakly influenced by the large scale signature of the uncertainty in the boundary conditions. In this section we only summarize the main elements of the inversion system, starting with the theoretical framework, while the detailed description can be found in Broquet et al. (2011).

We define the control vector \mathbf{x} of the atmospheric inversion as the 6-hour and $0.5^\circ \times 0.5^\circ$ mean NEE and ocean fluxes. The atmospheric inversion seeks the mean \mathbf{x}_a and covariance matrix \mathbf{A} of the normal distribution $N(\mathbf{x}_a, \mathbf{A})$ of the knowledge on \mathbf{x} based on (i) the atmospheric transport model, (ii) the prior knowledge \mathbf{x}_b of \mathbf{x} , (iii) the hourly mean atmospheric measurements \mathbf{y} , (iv) and v) the covariances \mathbf{B} and \mathbf{R} of the distributions of the prior uncertainty and of the observation error assuming that these uncertainties are normal and unbiased (i.e., equal to $N(0, \mathbf{B})$ and $N(0, \mathbf{R})$ respectively), and (vi) a Bayesian relationship between these distributions. The observation error is the combination of all sources of misfit between the atmospheric transport model and the concentration measurements other than the prior uncertainty, in particular the measurement errors, the model transport, aggregation and representation errors, and the errors from the model inputs that are not controlled by the inversion.

With this theoretical framework, \mathbf{x}_a is the minimum of the quadratic cost function $J(\mathbf{x})$ (Rodgers, 2000):

$$J(\mathbf{x}) = \frac{1}{2}(\mathbf{x} - \mathbf{x}_b)^T \mathbf{B}^{-1}(\mathbf{x} - \mathbf{x}_b) + \frac{1}{2}(H(\mathbf{x}) - \mathbf{y})^T \mathbf{R}^{-1}(H(\mathbf{x}) - \mathbf{y}) \quad (1)$$

where T denotes the transpose, and where H is the affine observation operator which maps the 6-hour (00:00-06:00, 06:00-12:00, 12:00-18:00 and 18:00-24:00; UTC time is used hereafter) and $0.5^\circ \times 0.5^\circ$ mean NEE and ocean CO_2 fluxes \mathbf{x} to the observational space based on the linear CO_2 atmospheric transport model with fixed open boundary conditions, and with fixed estimates of the anthropogenic fluxes and natural fluxes at resolutions higher than 6-hour and 0.5° ; $H: \mathbf{x} \rightarrow H(\mathbf{x})$ can be rewritten $H: \mathbf{x} \rightarrow \mathbf{H}\mathbf{x} + \mathbf{y}_{fixed}$ where \mathbf{y}_{fixed} is the signature, through atmospheric transport, of the fluxes (in particular the anthropogenic emissions) and boundary conditions not controlled by the inversion. \mathbf{H} is the combination of two linear operators: the first operator distributing 6-hour mean natural fluxes at the 1-hour resolution, and the second operator simulating the atmospheric transport from the 1-hour resolution fluxes at 0.5° resolution.

The inversion system derives an estimate of \mathbf{x}_a by performing an iterative minimization of $J(\mathbf{x})$ with the M1QN3 algorithm of Gilbert and Lemaréchal (1989). The gradient of J is derived using the adjoint operator of \mathbf{H} thanks to the availability of the adjoint version of the CHIMERE code. The covariance of the posterior uncertainty in inverted NEE \mathbf{A} , of main interest for this study, is given by the formula:

$$\mathbf{A} = (\mathbf{B}^{-1} + \mathbf{H}^T \mathbf{R}^{-1} \mathbf{H})^{-1} \quad (2)$$

This equation demonstrates the point raised in the introduction for justifying the OSSE framework, that \mathbf{A} does not depend on the observations or on the prior flux values themselves but only on their error covariance matrices, on the observation network density and stations location, and on the atmospheric transport operator. This allows assessing the performance of any observation system, whether existing or not. Of note is also that this calculation does not depend on $\mathbf{y}_{\text{fixed}}$, i.e., on the boundary conditions or on the anthropogenic fluxes in the domain so that such components can be ignored for the estimate of \mathbf{A} .

In this framework, a common performance indicator is the theoretical uncertainty reduction for specific budgets of the NEE estimates (averages over specified periods of time and over specified spatial domains), defined by:

$$\gamma = 1 - \frac{\sigma_a}{\sigma_b} \quad (3)$$

where σ_a and σ_b are the standard deviations of the posterior and prior uncertainties in the corresponding integrals in time and space (over the given periods of time and spatial domains) of the 6-hour and 0.5° resolution NEE field. If the observations perfectly constrain the inversion of a given budget of NEE, then $\gamma = 1$. On the opposite, if it does not bring any information to reduce the error from the prior, $\gamma = 0$. By definition, γ is a quantity relative to the uncertainty in the prior fluxes, which depends on the type of prior information on NEE that is expected to be used (estimates from a biosphere model in our case, see below Sect. 2.2.2). Of note is that the scores

of uncertainty and of uncertainty reduction given in this study refer to the standard deviation of the uncertainty in a specific budget of NEE, and that, hereafter, the term “standard deviation” is generally omitted.

Due to the size of the observation and control vectors in this study, we could not afford the analytical computation of Eq. (2) based on the full computation of the \mathbf{H} matrix (using a very large number of CHIMERE simulations; Hungershoefer et al., 2010). Instead we use the Monte Carlo approach of Chevallier et al. (2007) to compute \mathbf{A} . In this approach, an ensemble of posterior fluxes \mathbf{x}_{ai} is derived from an ensemble of inversions using synthetic prior flux \mathbf{x}_{bi} and data \mathbf{y}_i whose random errors ($\mathbf{x}_{bi}-\mathbf{x}_{true}$ and $\mathbf{y}_i-\mathbf{H}\mathbf{x}_{true}$ respectively) to a known truth (\mathbf{x}_{true} , whose value does not influence the results analyzed here, and which is thus ignored hereafter) sample the distributions $N(0, \mathbf{B})$ and $N(0, \mathbf{R})$. \mathbf{A} is obtained as the statistics of the posterior errors $\mathbf{x}_{ai}-\mathbf{x}_{true}$. The practical size of the ensemble is described below and its determination follows the discussion by Broquet et al. (2011). The convergence of the estimate of the inverted NEE for each inversion and the convergence of the statistics of the ensemble are necessary to ensure that the \mathbf{A} matrix computed with this method corresponds to the actual covariance of the posterior uncertainty given by Eq. (2). These convergences cannot be perfect with a limited number of iterations for the minimization algorithm and a limited number of inversion experiments in the Monte Carlo ensemble imposed by computational limitations. Therefore the estimate of \mathbf{A} can depend on parameters other than \mathbf{H} , \mathbf{B} and \mathbf{R} in practice, i.e., the numbers of iterations and of inversion experiments. However, it has been checked (see below Sect. 2.2.2) that the convergence is sufficient so that this dependence should not be significant for the quantities of interest.

2.2.2 Practical set-up

Atmospheric transport model

In this study, the operator \mathbf{H} is based on the CHIMERE mesoscale atmospheric transport model (Schmidt et al., 2001) forced with ECMWF winds. We use a configuration with a $0.5^\circ \times 0.5^\circ$ horizontal grid and with 25 σ -coordinate vertical levels starting from the surface and with a ceiling at ~ 500 hPa (such a ceiling being usual for regional transport modeling when focusing on mole fractions close to the ground, e.g. Marécal et al. 2015). The spatial extent of the corresponding domain is described below. CHIMERE is an off-line transport model. Hourly mass-fluxes are provided by the analyses of the European Centre for Medium-Range Weather Forecasts (ECMWF). The relatively high vertical and horizontal resolutions of CHIMERE allow a good vertical discretization of the Planetary Boundary Layer (PBL; the first 14 levels are below 1500 meters) along with a good representation of the orography and dynamics to match high frequency observations better than with global configuration whose typical horizontal resolution is $\sim 3^\circ$ (Peylin et al. 2013).

Spatial and temporal domains

In this study, we use the European domain shown in Fig. 1a which covers most of the European Union and some of Eastern Europe, with a land surface area of $6.8 \times 10^6 \text{ km}^2$. Its southwest corner is at 35°N and 15°W , and its northeast corner is at 70°N and 35°E . Two temporal windows are considered, from June 30, 2007 to July 20, 2007 and from 2 to 22 of December 2007 (of almost three weeks each). The choice of those periods of three weeks is a tradeoff between widening the scope of the study and computational burden. The Monte Carlo-based flux uncertainty reduction calculations require large computing resources, while we test three different network configurations for two different months, and for different setups of the error covariance matrices. Three week experiments allow retrieving information about uncertainties at the two-week scale without being biased by edge effects, i.e., they allow accounting for the impact of uncertainties from the days before the 14 targeted days and for the impact of the assimilation of measurements

during the days after these 14 targeted days. Indeed, the advection of CO₂ throughout Europe can last more than three days, but the atmospheric diffusion ensures that the signature at ICOS sites of the NEE during a 6-hour window is generally negligible after three days of transport (not shown). Thus, the windows 3-17 July and 5-19 December were chosen for analysis respectively. We consider the results for July and December to be representative for the summer and winter seasons, allowing an analysis of seasonal variations in the structure of the flux uncertainty reduction. Choosing year 2007 for the period of the inversion only impacts the meteorological conditions (i.e., the impact on the prior uncertainty whose local standard deviations are scaled using data from this specific year, as detailed below in this section, is negligible) and thus the atmospheric transport conditions in the OSSEs. We assume that these conditions are not impacted by a strong inter-annual anomaly in 2007 so that they can be expected to be representative of average conditions for summer and winter. Hereafter, the mention of the year 2007 is thus often ignored and we assume that we retrieve typical estimates for July and December.

Flux error covariance matrix

The setup of the error covariance matrix **B** follows the methodology of Chevallier et al. (2007). It is chosen to represent the typical uncertainty in estimates from the biosphere models (for NEE) and from climatologies (for ocean fluxes) used by traditional atmospheric inversion systems. The statistics have been derived more specifically for estimates from the Organising Carbon and Hydrology In Dynamic Ecosystems (ORCHIDEE) vegetation model (Krinner et al., 2005) and the ocean climatology from Takahashi et al. (2009). The uncertainties in NEE are assumed to be autocorrelated in space and in time and are modeled using isotropic and exponentially decreasing functions with correlation lengths that do not depend on the time or location. A Kronecker product of the matrices of temporal and spatial correlations ensures the combination of these two

types of correlations. The e-folding spatial and temporal correlation lengths are set according to the estimation of Chevallier et al. (2012) based on comparison of the NEE derived by the ORCHIDEE model and eddy-covariance flux tower data, for our specific prior flux spatial and temporal resolution, i.e., to 30 days in time and 250 km in space over land. NEE uncertainties for different 6-hour windows of the day are not correlated, i.e., the temporal correlations only apply to a given 6-hour window of consecutive days. The standard deviations of the prior uncertainties in **B** are set proportionally to the heterotrophic respiration fluxes from the ORCHIDEE model (it is approximately twice this respiration at the daily and 0.5° scale). We apply time-dependent scaling factors to these fluxes so that the NEE uncertainties have lower values during the night than during the day, and during winter than during summer, summing up to typical values for grid-scale and daily errors $\sim 2.5 \text{ gCm}^{-2}\text{day}^{-1}$ in summer (maximum value $3.4 \text{ gCm}^{-2}\text{day}^{-1}$) and $\sim 2 \text{ gCm}^{-2}\text{day}^{-1}$ in winter (maximum value $3.1 \text{ gCm}^{-2}\text{day}^{-1}$). Over the ocean, the prior uncertainty of air-sea fluxes has standard deviations at the 0.5° and 6-hour scale equal to $0.2 \text{ gCm}^{-2}\text{day}^{-1}$, an e-folding spatial correlation length of 500 km and temporal correlations similar to that for the prior uncertainties over land. Prior ocean and land flux uncertainties are not correlated.

Time selection of the data to be assimilated

Broquet et al. (2011) analyzed the periods of time during which the CHIMERE European configuration bears transport biases which are too high so that measurements from ground based stations such as ICOS sites should not be assimilated to avoid projecting erroneously such biases into the corrections to the fluxes. In agreement with common practice, they concluded that observations at low altitude sites (approximately below 1000 meters above sea level (masl); see Broquet et al. (2011) for the exact definition of the different types of sites used for the time selection of the data and the configuration of the observation error) which include almost all of the ICOS tall towers, should be assimilated during daytime (12:00-20:00) only while the

observations at high altitude stations (approximately above 1000 masl) should be used during the night (00:00-06:00) only. This generally yields larger uncertainty reduction during daytime than during nighttime (Broquet et al. 2011). However, this does not raise a potential bias related to a better constrain on daytime inverted NEE (when the ecosystems are generally a sink of CO₂) than on nighttime inverted NEE (when the ecosystems are generally a source of CO₂) since uncertainties in both nighttime and daytime prior NEE, transport and measurements are assumed to be unbiased, as supported by the results from Broquet et al. (2013).

Observation error covariance matrix

The observational error covariance matrix **R** accounts for various sources of error when comparing the hourly data selected for assimilation and their simulation which are not controlled by the inversion: measurement error, aggregation error, atmospheric model representativeness and transport error (as explained previously, uncertainties in the anthropogenic emissions and in the boundary conditions are assumed to be negligible). The first two terms are negligible compared to the model representativeness and transport error due to the high measurement standard and to solving for the fluxes at 6-hour and 0.5° resolution during the inversion, respectively.

Broquet et al. (2011) derived a quantitative estimation of the model error (depending on the station height) including transport and representativeness errors based on comparisons between simulations and measurements of CO₂ and ²²²Rn. Broquet et al. (2013) resumed it to provide season-dependent estimates which are used here. The model error is much higher during the winter than that during the summer. It is given for each site in Table A1 for the two months (July, December) considered in this study. We assume that the errors for two different sites are independent and that they do not bear temporal autocorrelations. Thus, the observation error covariance matrix **R** is set diagonal. Indeed, there is no evidence that such autocorrelations could

be significant in the analysis of Broquet et al. (2011). The resulting budget of observation errors at daily to monthly resolution seems reliable (Broquet et al. 2011, 2013). It could be due either to a compensation of ignoring the temporal autocorrelations by an overestimate of errors for hourly data, or to the fact that the temporal auto-correlations of actual observation are negligible (Broquet et al. 2013). However, in both cases, the assumption that the temporal autocorrelations of the observation error are negligible does not seem to need to be balanced by an artificial increase of the observation errors for hourly averages.

Minimization and number of members in the Monte Carlo ensembles

We use 12 iterations of minimization for each variational inversion of the Monte Carlo ensemble experiments. This number is similar to that from Broquet et al. (2011) where they considered a longer time period for the inversions but far smaller observation networks and a smaller inversion domain, which reduces the dimensions of the minimization problem. However, here, 12 iterations were still found to be sufficient for converging toward the theoretical minimum of the cost function, i.e., the number of assimilated data divided by two (Weaver et al., 2003), with less than 10% relative difference to this theoretical minimum except for few cases (for these cases, 18 iterations were used to reach a relative difference to the theoretical minimum that is smaller than 10%).

Similarly to Broquet et al. (2011), 60 members are used in each Monte Carlo ensemble experiment (this is also the typical number of members that Bousserez et al. 2015 use for their Monte Carlo simulations)."

. They found a satisfactory convergence of the estimate of the uncertainties in Europe and 1-month average NEE, with such a size of the ensemble which is confirmed here (the estimates using 50 and more members are within 6% of the results with 60 members).

446

447 **2.2.3 Sensitivity tests**

448 Three and five Monte Carlo ensembles of inversions are conducted for December and July
449 respectively. For each season, 3 ensembles using the default set-up of **B** and **R** described above
450 are conducted in order to give results for the 3 different ICOS network configurations and
451 consequently the sensitivity to the network configuration. In July, two ensembles are also
452 conducted with a change in **R** in one case and in **B** in the other case in order to test the sensitivity
453 to these inversion parameters. Such sensitivity tests have been conducted in July only and using
454 one configuration of the ICOS network only (ICOS50 and ICOS66 for the test of sensitivity to **R**
455 and **B** respectively) since a more exhaustive set of tests of sensitivity for the two seasons and for
456 each ICOS network configuration was not expected to bring new insights while raising
457 significant additional computation costs. The set-up of the inversion for these two sensitivity
458 tests is now described.

459

460 **Test of the sensitivity to the observation error**

461 There is a steady increase in the resolution of the atmospheric transport models used for
462 atmospheric inversions, with corresponding improvements of the simulation precision (e.g., Law
463 et al. 2008). In this test we simulate the effect of potential future transport model improvement
464 on the posterior flux uncertainties by reducing the default observation error standard deviations
465 in **R** by a factor of two. This factor roughly corresponds to the improvement of the misfits
466 between the model and actual measurement at the site TRN (see Fig. 1 for its location), that was
467 observed when bringing CHIMERE from the current 0.5° resolution down to a 2 km resolution
468 using the configuration presented in Bréon et al. (2014). The underlying assumption would be
469 that ~1km horizontal resolution atmospheric transport models could be used for inversions at the

European scale in the near future. Hereafter, we denote by \mathbf{R}_{ref} the reference configuration of \mathbf{R} and by \mathbf{R}_{red} the one corresponding to reduced standard deviations.

Test of the sensitivity to the prior uncertainty

The test of the sensitivity of the inversion system to the prior uncertainty is focused on that of the sensitivity to the spatial correlation length in \mathbf{B} (Gerbig et. al. 2006) (which impacts the budget of uncertainty over large regions). The possible use of better prior flux fields based on the merging of both estimates from vegetation models and from large scale inventories (such as forest and agricultural inventories) can be expected to generate smaller-scale uncertainties than when using vegetation models while it is not obvious that local uncertainties would be decreased when adding information from inventories (since inventories only measure long term integrated NEE). Therefore, we tested the impact of reducing the spatial correlation length for the prior uncertainty in NEE from 250 km to 150 km, denoting hereafter the corresponding configurations for the \mathbf{B} matrix: \mathbf{B}_{250} and \mathbf{B}_{150} respectively.

3. Results and discussion

3.1 Assessment of the performance of the actual network and system

In this section, the performance of the inversion relying on the default configuration and on the ICOS23 initial state network (i.e., the reference inversion) is analyzed as a function of the spatial scale, highlighting the main patterns of the uncertainty reduction obtained at the pixel scale to the European scale.

3.1.1 Analysis at the model grid scale

Figures 2a and 2b show the uncertainty reduction for estimates of two-week average NEE at 0.5° resolution in July and December, respectively. This grid-scale uncertainty reduction reaches 65% for areas in the vicinity of the ICOS sites and decreases smoothly with distance away from measurement sites. For most of the area around eastern France – western Germany, this grid – scale uncertainty reduction ranges from 35 to 50% for July and from 20 to 40% for December. This stems from the combination of the dense observation network over that region, and from the 250 km correlation scale for the prior uncertainties, which spreads the error reduction beyond the immediate vicinity of each station where near field fluxes have a large influence on the mixing ratio at this station (Bocquet, 2005). For other parts of Europe that are not well sampled by ICOS, significant uncertainty reductions are generally seen around each site but there are large areas where the inversion has no impact at the grid scale: Scandinavian countries, the eastern part of Germany, Poland, the south of the Iberian Peninsula and almost all of Eastern Europe.

The spatial structure of the uncertainty reduction and the underlying spatial extrapolation from a site is a complex combination of transport influence and of the structure of the prior uncertainty. Due to varying transport conditions, standard deviation of the prior uncertainty at the grid scale (which is larger in summer, see below the comments on Fig. 3), and observation error (which is larger in winter), the spatial distribution of uncertainty reduction is found to vary from summer to winter. Because the prior uncertainties are larger and the observation errors are smaller in July than in December, there is generally a larger uncertainty reduction in July (especially in Western Europe). But variations in meteorology alter (limiting or enhancing) this general behavior. The lower vertical mixing (which strengthens the sensitivity of the near ground measurements to the local fluxes) partly balances the higher observation error in December and the range of local uncertainty reductions overlaps between July and December. The observations from the Angus tall tower (**tta** site, Table A1) in Scotland or from Pallas (**pal** site, Table A1) in Finland contribute differently to the uncertainty reduction during July and December (using meteorological conditions from 2007), showing better performance at the grid scale during

summer. This also comes from the different weather regimes, with different dominant wind directions, different average wind speed and different vertical mixing in summer and winter. Regions lacking stations in ICOS23 have an uncertainty reduction which is more sensitive to the atmospheric transport than regions with a dense network. The uncertainty reduction in December is significantly larger in the east and in the southeast part of domain compared to July, due to more occurrences of winds from the east during December than during July.

Complementing the uncertainty reduction, Fig. 3 shows prior and posterior uncertainty standard deviations at the grid scale in order to illustrate the precision of the estimates of NEE that should be achievable with the reference inversion using the ICOS23 network. As already stated, prior uncertainties are up to $\sim 3 \text{ gCm}^{-2}\text{day}^{-1}$ (Fig. 3a) but the winter values are smaller than the summer ones (due to a weaker activity of the ecosystems; Fig. 3b). During both July and December, the uncertainties in two-week mean NEE in the regions that are best covered by observations (most of Western Europe) at 0.5° resolution are reduced by the inversion down to typical values of $\sim 1.5 \text{ gCm}^{-2}\text{day}$ (Fig. 3c,d).

3.1.2 Analysis at national scale

Figures 4a and 4b show the uncertainty reduction for two-week-and country-mean NEE in July and December respectively. The countries and corresponding estimates of prior and posterior uncertainties are listed in Table A2. The results suggest the ability of the mesoscale inversion framework to derive estimates of the NEE at the national scales with relatively low uncertainties. The uncertainty reduction is particularly large for countries such as Germany, France and the UK e.g., more than 80% for France during July. It is larger than 50% for a large majority of the countries in Western Europe and Scandinavia both in July and December.

The smallest uncertainty reduction applies to southeastern European countries where it can be smaller than 10 % (e.g., for Greece in July) indicating that the presence of stations very close to or within a given country is a requisite for bringing significant improvement to the estimates of NEE in this country. In general, the differences of the inversion skill between July and December look consistent with what has been analyzed at the pixel scale. In particular the uncertainty reduction is higher in July for western countries but higher in December for eastern countries for the same reasons as that given when analyzing the same behavior at the pixel scale.

3.1.3 Analysis at the European scale

Table 1 shows that the uncertainty in two-week-mean NEE in July averaged over the full European domain (6.8×10^6 km² of land surface) is reduced by the inversion by 50% down to a value of ~ 43 TgCmonth⁻¹ (see Table 1 for details) using the default configuration. The uncertainty reduction for December is 66%, resulting in a posterior uncertainty of ~ 26 TgCmonth⁻¹. The uncertainty reduction for the whole European domain is thus higher in December than in July. More precisely, while easterly winds in December strongly favor this period in terms of uncertainty reduction in Eastern Europe, the uncertainty reduction for NEE averaged over the reduced western European domain defined in Fig. 1c does not vary significantly with the season (66% and 64% for July and December respectively). This lack of seasonal variation of the uncertainty reduction at the scale of the western European domain (where most of the ICOS23 stations are located) seems to contrast with the grid-scale and national scales estimations in this domain which indicated that the uncertainty reduction is generally significantly higher during summer than during winter. This contrast will be analyzed and interpreted in the following Sect. 3.1.4.

3.1.4 Analysis of the variations of the uncertainty as a function of the spatial aggregation of the NEE: interpretation of the results obtained at the national and European scales

In order to examine here the dependency of the NEE uncertainty reduction to increasing spatial scales of aggregation for the analyses in July and December, we chose five locations at which we define centered areas with increasing size for which uncertainties in the average NEE are derived. These stations are located using the green circles in Fig. 1c. The five locations correspond to three observing sites of ICOS23: Trainou (TRN), Ochsenkopf (OXK), Plateau Rosa (PRS); one site of ICOS50: SMEAR II-ICOS Hyytiälä (HYY); and one point in Sweden which does not correspond to any site of the ICOS networks tested here, called SW1 hereafter (Fig. 1c). We compute the uncertainty reductions of the two-week mean NEE for July and December over 5 square (in degrees) domains centered around each site of $1.5^\circ \times 1.5^\circ$, $2.5^\circ \times 2.5^\circ$, $3.5^\circ \times 3.5^\circ$, $4.5^\circ \times 4.5^\circ$ and $10.5^\circ \times 10.5^\circ$ size (which corresponds to surfaces of different size in terms of km^2). Depending on their location and on their size, the corresponding domains expand over areas of Europe that are more or less constrained by the inversion at the pixel scale. But the variations of the uncertainty reduction when increasing the size of these domains are also strongly driven by the spatial correlations in the prior and posterior uncertainty. The results are displayed in Fig. 5.

The five locations used for this analysis are representative of the diversity of the situation regarding the differences between grid scale uncertainty reduction in July and in December. While the uncertainty reduction is slightly larger in July than in December for TRN, much larger in July for PRS and HYY, it is slightly larger in December at OXK and much larger in December at SW1. Furthermore, the values for these grid scale uncertainty reductions range from 15% to 50% in July and from 7% to 47% in December at these locations (Fig. 5).

The maximum scores of uncertainty reduction occur for spatial scales of aggregation ranging from 10^5 km^2 to 10^6 km^2 when considering the sites located in Western Europe. These scales

approximately correspond to the range of the sizes of the European countries and it is larger than the typical area of correlation of the prior uncertainty (as defined by prior correlation lengths of 250 km). Increasing the spatial resolution generally increases the uncertainty reduction since posterior uncertainties have generally smaller correlation lengths than prior uncertainties, due to the spatial attribution error when trying to link the measurement information to local fluxes despite the atmospheric mixing. This explains the increase of uncertainty reduction from the grid scale to the “national scales”. This also explains why, for a given regional density of the measurement network, larger countries bear larger uncertainty reductions (Fig. 4). However, above such national scales, the corresponding domains include parts of Eastern Europe being poorly sampled by the ICOS23 network which explains the decrease in uncertainty reduction.

The convergence of the results around TRN, PRS and OXK to nearly 65% uncertainty reduction in both December and July for the western European domain, and of the results at all sites to 53% in July and 66% in December for the whole Europe, when increasing the spatial averaging area, starts between the same 10^5km^2 and 10^6km^2 (national scale) averaging areas. For smaller areas, the differences between July and December or between different spatial locations stay similar to what is seen at the $0.5^\circ \times 0.5^\circ$ scale.

The similarity of the results for the western European domain despite differences at the grid scale in July and December can be explained by differences of correlations between areas at scales similar or larger than the national scale in the posterior uncertainties (since the correlations of the prior uncertainties aggregated at the national scale or at larger scales are very close for July and December). Figure 6 illustrates the variations of such correlations of the posterior uncertainty at the national scale between July and December using the example of correlations between Germany and other countries. These correlations are usually more negative in December, which indicates a larger difficulty in December than in July to distinguish in the information from the measurement network the separate contributions of the different neighboring countries (or of

different areas of larger size). This can be attributed to the stronger winds in December which increase the extent of the flux footprints of the concentration measurements. Such an increase of the footprints in December limit the ability to solve for the fluxes in the vicinity of the measurement sites but increase the ability to solve for the fluxes at large scales.

3.2 Impact of the extension of the ICOS network

The effect on local (grid scale) uncertainty reduction of assimilating data from new sites in the ICOS network depends on the coverage of the area by the initial ICOS23 network, as illustrated by the comparison of the results using ICOS23, ICOS50 and ICOS66 and the reference configuration of the inversion (see Fig. 2 and 7). For example, adding one new site in Sweden or Finland yields a stronger increase of the uncertainty reduction than adding one site in the central part of Western Europe, where the network is already rather dense. Since most of the new sites from ICOS23 to ICOS50 and then ICOS66 are located in Western Europe, the improvements due to adding 27 or 43 sites to ICOS23 do not thus appear to be as critical as what can be achieved using the 23 sites of ICOS23. Still, the changes from ICOS23 to ICOS50 significantly enhance the uncertainty reduction at 0.5° resolution even in Western Europe in July, e.g., with uncertainty reduction increased from ~40% using ICOS23 to ~60% using ICOS66 in Switzerland. The impact of adding new sites is larger in December than in July, and, consequently, results for western Germany and Benelux quite converge between July and December when increasing the network to ICOS66.

The impact on the scores of uncertainty reduction of the increase of the ICOS network is also significant at the national (compare Fig. 4 and Fig. 8) and European scales (see Table 1 and Fig. 9) when comparing results with ICOS50 or ICOS66 to those obtained with ICOS23. The ICOS66 network delivers uncertainty reductions as high as 80% for countries like France and Germany in July. For Europe, the uncertainty reduction when using ICOS66 reaches 79% down

to $\sim 15 \text{ TgCmonth}^{-1}$ posterior uncertainty in December, and 64% down to $\sim 33 \text{ TgCmonth}^{-1}$ posterior uncertainty in July. However, the increase from ICOS50 to ICOS66 does not seem to impact much the uncertainty reduction at these scales, especially in July.

Figure 9 illustrates the diversity (depending on the space locations) of the evolution of the impact of increasing the network as a function of the NEE averaging spatial scale. For a low altitude site already present in the dense part of ICOS23, the impact of adding new sites increases when increasing the spatial scale of the analysis up to areas where ICOS23 is less dense (mainly in Eastern Europe) and where new sites are included in ICOS50. The impact also increases for SW1 (which is located in the northeastern border of the domain) with increasing spatial aggregation scale since encompassing more and more of the new sites from ICOS23 to ICOS50 when extending the averaging domain to the European western area. But on the opposite, the impact of the addition of new sites can decrease when increasing the NEE spatial aggregation scale, e.g., at HYY where a new site is specifically added in ICOS50.

3.3 Sensitivity to the correlation length of the prior uncertainty

The impact of reducing the correlation e-folding length (from 250 km to 150 km) of the prior uncertainty in the inversion configuration is tested using ICOS66 in July (compare Fig. 7b and 10a, Fig. 8b and 11a, and the corresponding curves in Fig. 9). Such a change of correlation length strongly decreases the values of uncertainty reduction at all spatial scales. This is because it decreases the prior uncertainty at every scale while decreasing the ability of the inversion system to extrapolate in space the information from measurement sites based on the knowledge about spatial correlations of the prior uncertainties. At 0.5° resolution, the areas of high uncertainty reduction narrows around the measurement sites and the smaller overlap of the areas of influence of these sites limits the highest local values of uncertainty reduction to 40%-50% while typical values in Western Europe now range from 20% to 40% instead of 30% to 65%

when using \mathbf{B}_{250} (see Sect. 2.2.2 for the definition of the \mathbf{B} matrices). The uncertainty reduction for countries such as the UK, Germany and Spain decreases when the e-folding correlation length is lowered from 250 km to 150 km, from more than 75%-80% to less than 70%. For the full European domain, it decreases from 64% to 47%.

Even though these decreases can be very large, it is critical to keep in mind that they refer to uncertainty reductions compared to a prior uncertainty which is decreased by the new configuration of \mathbf{B} (as illustrated at the country scale in Fig. A1). The posterior uncertainty in the European and two-week mean NEE in July using ICOS66 is decreased from $\sim 33 \text{ TgC month}^{-1}$ to $29 \text{ TgC month}^{-1}$ when changing the configuration of \mathbf{B} from \mathbf{B}_{250} to \mathbf{B}_{150} (Table 1). Similarly, the posterior uncertainty is generally smaller at the national scale when changing the configuration of \mathbf{B} from \mathbf{B}_{250} to \mathbf{B}_{150} (Fig. A2). We thus have an expected situation for which improving the knowledge on the prior NEE improves that of the posterior NEE even if in our case, the improvement of the knowledge on the prior NEE which is tested here also decreases the ability to extrapolate in space the information from the atmospheric measurements. However, of note is that when changing the configuration of \mathbf{B} from \mathbf{B}_{250} to \mathbf{B}_{150} , we do not improve the knowledge on the prior NEE at the model grid 0.5° resolution (since modifying the correlations but not the standard deviations in \mathbf{B}). Given the lower uncertainty reduction when using \mathbf{B}_{150} , the posterior uncertainties are higher at 0.5° resolution when changing the configuration of \mathbf{B} from \mathbf{B}_{250} to \mathbf{B}_{150} (Fig. A3).

3.4 Sensitivity to the observation error

The impact of dividing the standard deviation of the observation error by two in the inversion configuration is tested using ICOS50 in July (compare Fig. 7a and 10b, Fig. 8a and 11b and the corresponding curves in Fig. 9). The decrease of observation error increases the weight of the measurements in the inversion and the resulting uncertainty reduction. This increase is visible at

all spatial scales for the aggregation of the NEE, and relatively constant as a function of these spatial scales except at the European scale for which it is quite smaller, from 64% to 67%. This provides the highest scores of uncertainty reduction of this study at any spatial scales, the impact of division of the observation error by two being larger than that of increasing the ICOS network configuration from ICOS50 to ICOS66.

4 Synthesis and conclusions

We assessed the potential of CO₂ mole fraction measurements from three configurations of the ICOS atmospheric network to reduce uncertainties in two-week mean European NEE at various spatial scales in summer and in winter. This assessment is based on a regional variational inverse modeling system with parameters consistent with the knowledge on uncertainties in prior estimates of NEE from ecosystem models and in atmospheric transport models. The results obtained with the various experiments from this study indicate an uncertainty reduction which ranges between ~50% and 80% for the full European domain, between ~70% and 90% for large countries in Western Europe (such as France, Germany, Spain, UK), where the ICOS network are denser, but below 50% in much cases for eastern countries where there are few ICOS sites even with the ICOS66 configuration. At 0.5° resolution, if excluding results when using \mathbf{B}_{150} (for which the uncertainty reduction is applied to a different prior uncertainty), uncertainty reductions range from 30% to 65% in the dense parts of the networks (between northern Spain and eastern Germany) while it is generally below 30% east of Germany and Italy when using ICOS23 or east of Poland and Hungary when using ICOS66. The very high values of uncertainty reduction obtained in areas where ICOS sites are distant by less than the typical length scale of the prior uncertainty (Western Europe when using ICOS23 and a larger area when using ICOS66) is highly promising.

Despite the absence of seasonal variation for the uncertainty in the average NEE over Western Europe (at least according to our results for the year 2007) significant seasonal variations at higher resolution or for the full European domain reveal the influence of the atmospheric transport on the scores of uncertainty reduction. Using ICOS66 instead of ICOS23 does not limit this behavior since few sites are added between ICOS23 and ICOS66 in Eastern Europe where the largest seasonal variations of the uncertainty reduction occur. The impact of the larger wind speed in December yielding similar uncertainty reduction in July and December for Western Europe also highlights the influence of the atmospheric transport on the scores of uncertainty reduction. It demonstrates that such scores and their sensitivity to the network extension are not fully intuitive and that their derivation requires such a complex application of an inversion system as in this study.

These scores of uncertainty reduction result in posterior uncertainties lower than $1.8 \text{ gC m}^{-2} \text{ day}^{-1}$ at 0.5° resolution in the areas where the ICOS network is dense. At the national scale, posterior uncertainties scales are compared to the typical estimates of the NEE from the ORCHIDEE model for the corresponding two-week period in July 2007 in Table A2. The relative posterior uncertainty could be less than 20% for the countries gathering the largest NEE such as France, Germany, Poland or UK (if using ICOS66 in the three last cases, otherwise it should be less than 30% if using ICOS23), even though it would not be the case for Scandinavian countries with a high NEE too. For some Eastern European countries, the posterior uncertainty could be very close to the estimate of NEE from ORCHIDEE but the general tendency is to obtain posterior uncertainties much lower than the estimate of the NEE from ORCHIDEE even when using ICOS23. This tendency is reflected at the European scale (Table 1) for which the posterior uncertainty when using ICOS23 and the reference inversion configuration is $\sim 20\%$ and $\sim 30\%$ of the total NEE from ORCHIDEE in July and December respectively. These numbers can be compared to the uncertainty targets defined for the CarbonSat satellite mission (ESA, 2015): $0.5 \text{ gC m}^{-2} \text{ day}^{-1}$ at the $500 \text{ km} \times 500 \text{ km}$ and 1 month scale. Figures 12, A1 and A2 shows that at

the 2-week and national scale, the prior uncertainties are systematically well larger than this target, but that the posterior uncertainties in Western and Northern Europe are generally close or smaller than this target even when using ICOS23. Since the temporal correlations in the prior uncertainty have a 1 month timescale and since the temporal correlations in the posterior uncertainty should be smaller, these uncertainties at the 2-week scale can be considered to be equal or lower than the corresponding uncertainties at the 1 month scale. Therefore, this indicates that the inversion is required to reach the target from the CarbonSat report for mission selection. It also indicates that this target is likely not reached in a large part of South Eastern Europe even when using ICOS66 but that for countries like the Czech Republic and Poland, extending the network from ICOS23 to ICOS66 allows reaching it. Finally, it indicated that the ICOS23 network is sufficient to reach this target in Western Europe.

The comparison of the sensitivity of the results in July to changes in the observation network, correlation lengths of the prior uncertainty and observation error (in the range of tests conducted in this study) indicates a different hierarchy of the impact of such changes depending on the spatial scales. Increasing the network from ICOS23 to ICOS50 yields the largest change in posterior uncertainty due to a significantly better monitoring of the eastern part of Europe. However, for western countries, at the grid to national scales, the impact of changing the inversion parameters is generally larger than that of the increase of the network. Given the range of spatial correlations in the prior uncertainty that are investigated here, the spacing of ICOS sites in Western Europe is already sufficiently narrow to ensure that this full domain is significantly constrained by the measurements from ICOS23. The weight of this constraint at grid to national scales in Western Europe is more directly modified by dividing by two the observation errors or shortening by nearly half the correlation length of the prior uncertainties than by doubling the number of monitoring sites.

The fact, in Western Europe, that notional targets for the posterior uncertainty in national scale NEE are already reached in Western Europe when using ICOS23, that the sensitivity of the posterior uncertainties at the national to 0.5° scale to increase in the network is relatively low, and the fact that results in Eastern Europe are highly impacted by the increase of the network encourage a spread of the ICOS network to poorly monitored areas rather than a densification of the core of this network in Western Europe. This recommendation sounds natural but this study would have rather supported a densification of the network in Western Europe if revealing that the density of the ICOS23 network was not high enough there, so that spreading the network in the East would have resulted in preventing from getting useful information about the NEE anywhere in Europe. These results also raise optimism regarding the benefits from improvements of the atmospheric transport modeling or from the improvement of the prior “bottom-up” (as opposed to the “top-down” information from atmospheric concentrations) knowledge on the fluxes.

Some limitations of the calculations should be kept in mind when analyzing the results more precisely. The convergence of the calculations as a function of the number of minimization iterations during the inversion or as a function of the number of inversions in each Monte Carlo ensemble experiment, has been assessed based on average diagnostics. Locally, some results have not converged. Additionally, the use of ICOS50 or ICOS66 should require more minimization iterations to converge to the same extent as when using ICOS23 or ICOS50 (respectively) due to the increase of the dimension of the inversion problem. As an example, this results in the diagnostic of very slight increases (which do not yield significant relative differences) of the posterior uncertainty for Sweden or for Europe when extending ICOS50 to ICOS66. Such problems seem very minor. They slightly alter the scores of uncertainty reduction for specific areas only, but they are not significant enough to impact the typical range of values analyzed and the subsequent conclusions in this study.

Another point is that the confidence in the reference configuration of the inversion has been built based on the diagnostics of the errors in NEE simulated with the ORCHIDEE model at the local scale from Chevallier et al. (2012) and at the monthly and Europe wide scale from Broquet et al. (2013). A simple model is used to represent the correlations of the prior uncertainty in NEE and thus the prior uncertainty in NEE at the intermediate scales. It may need to be refined to better account for the heterogeneity of the European ecosystems with potential impact on the results of posterior uncertainty at fine scales. Furthermore, the assumption that the uncertainties in CO₂ anthropogenic emissions do not have a significant signature at the ICOS sites is based on studies at relatively few monitoring sites corresponding to the coarse atmospheric network of the CarbonEurope-IP project (Schulze et al. 2010). When considering far denser networks with many sites close to urban areas (such as in and around the Netherlands when using ICOS66), this uncertainty should likely be accounted for. The assumption that uncertainties in the boundary conditions and in the anthropogenic emissions have a weak impact on the inversion is also supported on average by the results of Broquet et al. (2013). But when assessing results for specific areas such as in this study, this assumption may be weakened in highly industrialized countries or close to the model domain boundaries. Such considerations should lead to further investigation regarding the inversion configuration and thus potential refinement of the results.

This study focuses on results for two-week mean fluxes while a critical target of the inversion should be related to annual mean fluxes. This and the strong influence of the variations of the meteorological conditions on the inversion results (which limits the ability to extrapolate the results to the annual scale) encourage the set-up of 1-year long experiments. However, this study already gives qualitative insights on such results and on their sensitivity to the observing network or to accuracy of the different components of the system which should support future network design studies in Europe. By demonstrating the capability for deriving scores of uncertainty reductions for NEE at 6-hour and 0.5° resolution, it supports the development of operational

815 inversion systems deriving the optimal location for new sites to be installed in the European
816 network.

817

818

819

820

821

822

823

824

825

826

827

828

829

830

831

832

833

834

Acknowledgement

This study was co-funded by the European Commission under the EU Seventh Research Framework Programme (grant agreement No. 283080, Geocarbon project) and under the framework of the preparatory phase of ICOS. It was also co-funded by the industrial chaire BridGES (supported by the Université de Versailles Saint-Quentin-en-Yvelines, the Commissariat à l'Energie Atomique et aux Energies Renouvelables, the Centre National de la Recherche Scientifique, Thales Alenia Space and Veolia). We also would like to thank the partners of the ICOS infrastructure for providing list of potential locations for future ICOS atmospheric sites.

References

- Ahmadov, R., Gerbig, C., Kretschmer, R., Körner, S., Rödenbeck, C., Bousquet, P., and Ramonet, M.: Comparing high resolution WRF-VPRM simulations and two global CO₂ transport models with coastal tower measurements of CO₂, *Biogeosciences*, 6, 807-817, doi:10.5194/bg-6-807-2009, 2009.
- Bocquet, M.: Grid resolution dependence in the reconstruction of an atmospheric tracer source, *Nonlin. Processes Geophys.*, 12, 219–234, 2005.
- Bousserez, N., Henze, D. K., Perkins, A., Bowman, K. W., Lee, M., Liu, J., Deng, F., and Jones, D. B. A.: Improved analysis-error covariance matrix for high-dimensional variational inversions: application to source estimation using a 3-D atmospheric transport model, *Q. J. Roy. Meteor. Soc.*, doi:10.1002/qj.2495, 19021, 19023, 2015.
- Bréon, F. M., Broquet, G., Puygrenier, V., Chevallier, F., Xueref-Rémy, I., Ramonet, M., Dieudonné, E., Lopez, M., Schmidt, M., Perrussel, O., and Ciais, P.: An attempt at estimating Paris area CO₂ emissions from atmospheric concentration measurements, *Atmos. Chem. Phys.* 15, 1707-1724, doi:10.5194/acp-15-1707-2015, 2015.
- Broquet, G., Chevallier, F., Rayner, P. J., Aulagnier, C., Pison, I., Ramonet, M., Schmidt, M., Vermeulen, A. T., and Ciais, P.: A European summertime CO₂ biogenic flux inversion at mesoscale from continuous in situ mixing ratio measurements, *J. Geophys. Res.*, 116, D23303, doi:10.1029/2011JD016202, 2011
- Broquet, G., Chevallier, F., Bréon, F.-M., Kadygrov, N., Alemanno, M., Apadula, F., Hammer, S., Haszpra, L., Meinhardt, F., Morguí, J. A., Necki, J., Piacentino, S., Ramonet, M., Schmidt, M., Thompson, R. L., Vermeulen, A. T., Yver, C., and Ciais, P.: Regional inversion of CO₂ ecosystem fluxes from atmospheric measurements: reliability of the uncertainty estimates, *Atmos. Chem. Phys.*, 13, 9039-9056, doi:10.5194/acp-13-9039-2013, 2013.
- Chevallier, F., Bréon, F. M., and Rayner, P. J.: Contribution of the Orbiting Carbon Observatory to the estimation of CO₂ sources and sinks: Theoretical study in a variational data assimilation framework, *J. Geophys. Res.*, 112, D09307, doi:10.1029/2006JD007375, 2007.
- Chevallier, F., Wang, T., Ciais, P., Maignan, F., Bocquet, M., Arain A., Cescatti, A., Chen, J., Dolman, A. J., Law, B. E., Margo-lis, H., Montagnani, L., and Moors, E.: What eddy-covariance measurements tell us about prior land flux errors in CO₂-flux inversion schemes, *Global Biogeochem. Cycles*, 26, GB1021, doi:10.1029/2010GB003974, 2012.
- Claeyman, M., Attié, J.-L., Peuch, V.-H., El Amraoui, L., Lahoz, W. A., Josse, B., Joly, M., Barré, J., Ricaud, P., Massart, S., Piacentini, A., von Clarmann, T., Höpfner, M., Orphal, J., Flaud, J.-M. and Edwards, D. P.: A thermal infrared instrument onboard a geostationary platform for CO and O₃ measurements in the lowermost troposphere: Observing System Simulation Experiments (OSSE), *Atmos. Meas. Tech.*, 4, 1637-1661, doi:10.5194/amt-4-1637-2011, 2011.
- Edwards, D. P., Arellano Jr., A. F. and Deeter M. N.: A satellite observation system simulation experiment for carbon monoxide in the lowermost troposphere, *J. Geophys. Res.*, 114, D14304, doi:10.1029/2008JD011375, 2009.

- 910 Enting, I. G.: Inverse Problems in Atmospheric Constituent Transport, Cambridge Univ. Press,
911 Cambridge, U. K., 2002.
- 912
- 913 Errico, R. M., Yang, R., Privé, N. C., Tai, K.-S., Todling, R., Sienkiewicz, M. E. and Guo, J.:
914 Development and validation of observing-system simulation experiments at NASA's Global
915 Modeling and Assimilation Office. Q.J.R. Meteorol. Soc., 139: 1162–1178, doi: 10.1002/qj.2027,
916 2013.
- 917
- 918 ESA, Report for Mission Selection: CarbonSat, ESA SP-1330/1, (2 volume series), European
919 Space Agency, Noordwijk, The Netherlands, 2015.
- 920
- 921 Francey, R.J. (Ed.): Report of the Ninth WMO meeting of experts on carbon dioxide
922 concentration and related tracer measurement techniques. Aspendale, Vic., Australia, 1–4
923 September 1997, World Meteorological Organization (WMO), Geneva, Series: Global
924 Atmosphere Watch (GAW); no. 132; WMO; TD no. 952, 132 pp., 1998.
- 925
- 926 Gerbig, C., Lin, J. C., Munger, J. W., and Wofsy, S. C.: What can tracer observations in the
927 continental boundary layer tell us about surface-atmosphere fluxes?, Atmos. Chem. Phys., 6,
928 539-554, doi:10.5194/acp-6-539-2006, 2006.
- 929
- 930 Gilbert, J. C., and Lemaréchal, C.: Some numerical experiments with variable-storage quasi-
931 Newton algorithms, Math. Program., 45, 407–435, 1989.
- 932
- 933 Göckede, M., Turner, D. P., Michalak, A. M., Vickers, D. and Law B. E.: Sensitivity of a
934 subregional scale atmospheric inverse CO₂ modeling framework to boundary conditions, J.
935 Geophys. Res., 115, D24112, doi:10.1029/2010JD014443, 2010.
- 936
- 937 Gurney, K. R., Law, R. M., Denning, A. S., Rayner, P. J., Baker, D., Bousquet, P., Bruhwiler, L.,
938 Chen, Y.-H., Ciais, P., Fan, S., Fung, I. Y., Gloor, M., Heimann, M., Higuchi, K., John, J., Maki,
939 T., Maksyutov, S., Masarie, K., Peylin, P., Prather, M., Pak, B. C., Randerson, J., Sarmiento, J.,
940 Taguchi, S., Takahashi, T., and Yuen, C.-W.: Towards robust regional estimates of CO₂ sources
941 and sinks using atmospheric transport models, Nature, 415, 626–630, 2002.
- 942
- 943 Halliwell Jr., G. R., Srinivasan, A., Kourafalou, V., Yang, H., Willey, D., Le Hénaff, M. and
944 Atlas, R.: Rigorous Evaluation of a Fraternal Twin Ocean OSSE System for the Open Gulf of
945 Mexico. J. Atmos. Oceanic Technol., **31**, 105–130, doi: 10.1175/JTECH-D-13-00011.1, 2014.
- 946
- 947 Hourdin, F., Musat I., Bony S., Braconnot P., Codron F., Dufresne J. L., Fairhead L., Filiberti M.
948 A., Friedlingstein P., Grandpeix J. Y., Krinner G., LeVan P., Li Z.X., Lott F.: The LMDZ4
949 general circulation model: Climate performance and sensitivity to parametrized physics with
950 emphasis on tropical convection, J. Clim. Dyn., 27, 787–813, doi:10.1007/s00382-006- 0158-0,
951 2006.
- 952
- 953 Houweling, S., Breon, F.-M., Aben, I., Rödenbeck, C., Gloor, M., Heimann, M., and Ciais, P.:
954 Inverse modeling of CO₂ sources and sinks using satellite data: a synthetic inter-comparison of
955 measurement techniques and their performance as a function of space and time, Atmos. Chem.
956 Phys., 4, 523-538, doi:10.5194/acp-4-523-2004, 2004.
- 957
- 958 Hungershofer, K., Breon, F.-M., Peylin, P., Chevallier, F., Rayner, P., Klonecki, A.,
959 Houweling, S., and Marshall, J.: Evaluation of various observing systems for the global

- monitoring of CO₂ surface fluxes, *Atmos. Chem. Phys.*, 10, 10503-10520, doi:10.5194/acp-10-10503-2010, 2010.
- Kadygrov, N., Maksyutov, S., Eguchi, N., Aoki, T., Nakazawa, T., Yokota, T., and Inoue, G.: Role of simulated GOSAT total column CO₂ observations in surface CO₂ flux uncertainty reduction, *J. Geophys. Res.*, 114, D21208, doi:10.1029/2008JD011597, 2009.
- Krinner, G., Viovy, N., de Noblet-Ducoudré, N., Ogée, J., Polcher, J., Friedlingstein, P., Ciais, P., Sitch, S., and Prentice, I. C.: A dynamic global vegetation model for studies of the coupled atmosphere-biosphere system, *Global Biogeochem. Cycles*, 19, GB1015, doi:10.1029/2003GB002199, 2005.
- Lauvaux, T., Uliasz, M., Sarraz, C., Chevallier, F., Bousquet, P., Lac, C., Davis, K. J., Ciais, P., Denning, A. S., and Rayner, P. J.: Mesoscale inversion: first results from the CERES campaign with synthetic data, *Atmos. Chem. Phys.*, 8, 3459–3471, doi:10.5194/acp-8-3459-2008, 2008.
- Lauvaux, T., Schuh, A. E., Uliasz, M., Richardson, S., Miles, N., Andrews, A. E., Sweeney, C., Diaz, L. I., Martins, D., Shepson, P. B., and Davis, K. J.: Constraining the CO₂ budget of the corn belt: exploring uncertainties from the assumptions in a mesoscale inverse system, *Atmos. Chem. Phys.*, 12, 337-354, doi:10.5194/acp-12-337-2012, 2012.
- Law, R. M., Peters, W., Roedenbeck, C., Aulagnier, C., Baker, I., Bergmann, D. J., Bousquet, P., Brandt, J., Bruhwiler, L., Cameron-Smith, P. J., Christensen, J. H., Delage, F., Denning, A. S., Fan, S., Geels, C., Houweling, S., Imasu, R., Karstens, U., Kawa, S. R., Kleist, J., Krol, M. C., Lin, S. J., Lokupitiya, R., Maki, T., Maksyutov, S., Niwa, Y., Onishi, R., Parazoo, N., Patra, P. K., Pieterse, G., Rivier, L., Satoh, M., Serrar, S., Taguchi, S., Takigawa, M., Vautard, R., Vermeulen, A. T., and Zhu, Z.: TransCom model simulations of hourly atmospheric CO₂: Experimental overview and diurnal cycle results for 2002, *Global Biogeochem. Cycles*, 22, GB3009, doi:10.1029/2007gb003050, 2008.
- Marécal, V., Peuch, V.-H., Andersson, C., Andersson, S., Arteta, J., Beekmann, M., Benedictow, A., Bergström, R., Bessagnet, B., Cansado, A., Chéroux, F., Colette, A., Coman, A., Curier, R. L., Denier van der Gon, H. A. C., Drouin, A., Elbern, H., Emili, E., Engelen, R. J., Eskes, H. J., Foret, G., Friese, E., Gauss, M., Giannaros, C., Guth, J., Joly, M., Jaumouillé, E., Josse, B., Kadygrov, N., Kaiser, J. W., Krajsek, K., Kuenen, J., Kumar, U., Liora, N., Lopez, E., Malherbe, L., Martinez, I., Melas, D., Meleux, F., Menut, L., Moinat, P., Morales, T., Parmentier, J., Piacentini, A., Plu, M., Poupkou, A., Queguiner, S., Robertson, L., Rouil, L., Schaap, M., Segers, A., Sofiev, M., Tarasson, L., Thomas, M., Timmermans, R., Valdebenito, Á., van Velthoven, P., van Versendaal, R., Vira, J., and Ung, A.: A regional air quality forecasting system over Europe: the MACC-II daily ensemble production, *Geosci. Model Dev.*, 8, 2777-2813, doi:10.5194/gmd-8-2777-2015, 2015.
- Masutani, M., Schlatter, T. W., Errico, R. M., Stoffelen, A., Andersson, E., Lahoz, W., Woollen, J. S., Emmitt, G. D., Riishøjgaard, L.-P. and Lord, S. J.: “Observing System Simulation Experiments” in *Data Assimilation: Making sense of observations*, Eds. Lahoz, W. A., Khattatov B. and Ménard, R., Springer, Berlin, pp 647-679, 2010.
- Meesters, A. G. C. A., Tolk, L.F., Peters, W., Hutjes, R. W. A., Veling, O.S., Elbers, J.A., Vermeulen, A.T., van der Laan, S., Neubert, R. E. M., Meijer, H. A. J. and Dolman, A. J.: Inverse carbon dioxide flux estimates for the Netherlands, *J. Geophys. Res.*, 117, D20306, doi:10.1029/2012JD017797, 2012.

- Peters, W., Krol, M. C., Van Der Werf, G. R., Houweling, S., Jones, C. D., Hughes, J., Schaefer, K., Masarie, K. A., Jacobson, A. R., Miller, J. B., Cho, C. H., Ramonet, M., Schmidt, M., Ciattaglia, L., Apadula, F., Heltai, D., Meinhardt, F., Di Sarra, A. G., Piacentino, S., Sferlazzo, D., Aalto, T., Hatakka, J., Strom, J., Haszpra, L., Meijer, H. A. J., Van Der Laanm, S., Neubert, R. E. M., Jordan, A., Rodo, X., Morgui, J.-A., Vermeulen, A. T., Popa, E., Rozanski, K., Zimnoch, M., Manning, A. C., Leuenberger, M., Uglietti, C., Dolman, A. J., Ciais, P., Heimann, M. and Tans, P. P.: Seven years of recent European net terrestrial carbon dioxide exchange constrained by atmospheric observations. *Global Change Biology*, 16: 1317–1337. doi: 10.1111/j.1365-2486.2009.02078.x, 2010.
- Peylin, P., Houweling, S., Krol, M. C., Karstens, U., Rödenbeck, C., Geels, C., Vermeulen, A., Badawy, B., Aulagnier, C., Pregger, T., Delage, F., Pieterse, G., Ciais, P., and Heimann, M.: Importance of fossil fuel emission uncertainties over Europe for CO₂ modeling: model intercomparison, *Atmos. Chem. Phys.*, 11, 6607-6622, doi:10.5194/acp-11-6607-2011, 2011.
- Peylin, P., Law, R. M., Gurney, K. R., Chevallier, F., Jacobson, A. R., Maki, T., Niwa, Y., Patra, P. K., Peters, W., Rayner, P. J., Roedenbeck, C., van der Laan-Luijkx, I. T., and Zhang, X.: Global atmospheric carbon budget: results from an ensemble of atmospheric CO₂ inversions, *Biogeosciences*, 10, 6699-6720, doi:10.5194/bg-10-6699-2013, 2013.
- Rayner, P. J., Enting, I.G., and Trudinger, C. M.: Optimizing the CO₂ observing network for constraining sources and sinks, *Tellus B*, 48(4), 433-444, 1996.
- Riishojgaard, L. P., Ma, Z., Masutani, M., Woollen, J. S., Emmitt, G. D., Wood, S. A. and Greco, S.: Observation system simulation experiments for a global wind observing sounder, *Geophys. Res. Lett.*, 39, L17805, doi:10.1029/2012GL051814, 2012.
- Roedenbeck, C., Houweling, S., Gloor, M., and Heimann, M.: CO₂ flux history 1982–2001 inferred from atmospheric data using a global inversion of atmospheric transport, *Atmos. Chem. Phys.*, 3, 1919-1964, doi:10.5194/acp-3-1919-2003, 2003.
- Schmidt, H., Derognat, C., Vautard, R., and Beekmann, M.: A comparison of simulated and observed ozone mixing ratios for the summer of 1998 in Western Europe, *Atmos. Environ.*, 35(36), 6277–6297, doi:10.1016/S1352-2310(01)00451-4, 2001.
- Schuh, A. E., Denning, A. S., Corbin, K. D., Baker, I. T., Uliasz, M., Parazoo, N., Andrews, A. E., and Worthy, D. E. J.: A regional high-resolution carbon flux inversion of North America for 2004. *Biogeosciences* 7, 1625–1644, doi: 10.5194/bg-7-1625-2010, 2010.
- Schulze, E. D., Ciais, P., Luyssaert, S., Schrumpf, M., Janssens, I. A., Thiruchittampalam, B., Theloke, J., Saurat, M., Bringezu, S., Lelieveld, J., Lohila, A., Rebmann, C., Jung, M., Bastviken, D., Abril, G., Grassi, G., Leip, A., Freibauer, A., Kutsch, W., Don, A., Nieschulze, J., Börner, A., Gash, J. H., and Dolman, A. J.: The European carbon balance. Part 4: integration of carbon and other trace-gases fluxes, *Global Change Biol.*, 16, 1451–1469, 2010.
- Takahashi, T., Sutherland, S. C., Wanninkhof, R., Sweeney, C., Feely, R. A., Chipman, D. W., Hales, B., Friederich, G., Chavez, F., Sabine, C., Watson, A., Bakker, D. C. E., Schuster, U., Metzl, N., Yoshikawa-Inoue, H., Ishii, M., Midorikawa, T., Nojiri, Y., Körtzinger, A., Steinhoff, T., Hoppema, M., Olafsson, J., Arnarson, T. S., Tilbrook, B., Johannessen, T., Olsen, A., Bellerby, R., Wong, C. S., Delille, B., Bates, N. R., and de Baar, H. J. W.: Climatological mean and decadal change in surface ocean pCO₂, and net sea-air CO₂ flux over the global oceans, *Deep-Sea Research II* 56(8-10), pp. 554-577. doi:10.1016/j.dsr2.2008.12.009,

2009.

Timmermans, R. M. A., Schaap, M., Elbern, H., Siddans, R., Tjemkes, S., Vautard, R. and Builtjes, P.: An Observing System Simulation Experiment (OSSE) for Aerosol Optical Depth from Satellites. *J. Atmos. Ocean Tech.*, **26**, 2673-2682, 2009a.

Timmermans, R. M. A., Segers, A. J., Builtjes, P. J. H., Vautard, R., Siddans, R., Elbern, H., Tjemkes, S. A. T. and Schaap, M.: The added value of a proposed satellite imager for ground level particulate matter analyses and forecasts. *IEEE J. Sel. Top. Appl.*, **2**, 271–283, 2009b.

Tolk, L. F., Dolman, A. J., Meesters, A. G. C. A., and Peters, W.: A comparison of different inverse carbon flux estimation approaches for application on a regional domain, *Atmos. Chem. Phys.*, **11**, 10349-10365, doi:10.5194/acp-11-10349-2011, 2011.

Weaver, A.T., Vialard, J., Anderson, D.L.T, Delecluse, P.: Three- and four-dimensional variational assimilation with an ocean general circulation model of the tropical Pacific Ocean. Part I: formulation, internal diagnostics and consistency checks, *Mon. Wea.Rev.*, **131**, 1360-1378, 2003.

World Meteorological Organization: “Scientific Requirements” in Report of the WMO/UNEP/ICSU Meeting on Instruments, Standardization and measurement techniques for atmospheric CO₂, Geneva, Switzerland, 8-11 September 1981.

Zhang, X., Gurney, K. R., Rayner, P., Baker, D., and Liu, Y.-P.: Sensitivity of simulated CO₂ concentration to sub-annual variations in fossil fuel CO₂ emissions, *Atmos. Chem. Phys. Discuss.*, **15**, 20679-20708, doi:10.5194/acpd-15-20679-2015, 2015.

Ziehn, T., Nickless, A., Rayner, P. J., Law, R. M., Roff, G., and Fraser, P.: Greenhouse gas network design using backward Lagrangian particle dispersion modelling – Part 1: Methodology and Australian test case, *Atmos. Chem. Phys.*, **14**, 9363-9378, doi:10.5194/acp-14-9363-2014, 2014.

Table 1. Uncertainty reduction in two-week and European mean NEE for July and December as a function of the observation network and of the configuration of the inversion parameters (\mathbf{B}_{250} or \mathbf{B}_{150} for \mathbf{B} and \mathbf{R}_{ref} or \mathbf{R}_{red} for \mathbf{R}).

	Month	B	R	Prior uncertainty (TgCmonth ⁻¹)	Posterior uncertainty (TgCmonth ⁻¹)	NEE from ORCHIDEE (TgCmonth ⁻¹)	Uncertainty Reduction (%)
ICOS23	July	\mathbf{B}_{250}	\mathbf{R}_{ref}	91.2	42.6	-201.6	53
	December	\mathbf{B}_{250}	\mathbf{R}_{ref}	74.9	25.5	80.3	66
ICOS50	July	\mathbf{B}_{250}	\mathbf{R}_{ref}	91.2	32.4	-201.6	64
	December	\mathbf{B}_{250}	\mathbf{R}_{ref}	74.9	19.5	80.3	74
	July	\mathbf{B}_{250}	\mathbf{R}_{red}	91.2	30.4	-201.6	67
ICOS66	July	\mathbf{B}_{250}	\mathbf{R}_{ref}	91.2	32.8	-201.6	64
	December	\mathbf{B}_{250}	\mathbf{R}_{ref}	74.9	15.4	80.3	79
	July	\mathbf{B}_{150}	\mathbf{R}_{ref}	55.0	29.2	-201.6	47

Table A1. Atmospheric measurement sites for the different ICOS network configurations considered in this study with associated observation errors in the reference configuration of the inversion. Two values are given for the observation error at a given site for low altitude sites: that for temporal window 12:00-18:00 (left) and window 18:00-20:00 (right), and one value for window 00:00-06:00 at high altitude sites. Height corresponds to the vertical location of the site above the ground level (magl) and elevation corresponds to the vertical location of the ground above sea level at the site position.

Network	Site	Country	Code	type	Lon	Lat	Height magl	Elevation masl	Assim. Window	Obs. Err. (ppm)	
										July	Dec
ICOS23	Bialystok	PL	bik	TT	23.01	53.23	300	480	12-20	4.2-7.2	10.2-15.2
	Biscarrose	FR	bis	G	-1.23	44.38	47	120	12-20	4.2-7.2	10.2-15.2
	Cabauw	NL	cbw	TT	4.93	51.97	200	200	12-20	4.2-7.2	10.2-15.2
	Monte Cimone	IT	cmn	G	10.68	44.17	12	2177	00-06	3.6	3.6
	Gif-sur-Yvette	FR	gif	G	2.15	48.71	7	167	12-20	4.2-7.2	10.2-15.2
	Heidelberg	DE	hei	G	8.67	49.42	30	146	12-20	4.2-7.2	10.2-15.2
	Hegyhatsal	HN	hun	TT	16.65	46.96	115	363	12-20	4.2-7.2	10.2-15.2
	Jungfraujoch	CH	jfj	G	7.98	46.55	gl	3580	00-06	3.6	3.6
	Kasprowy Wierch	PL	kas	G	19.98	49.23	gl	1987	00-06	3.6	3.6
	Lampedusa	IT	lmp	G	12.63	35.52	8	58	12-20	4.2-7.2	10.2-15.2
	La Muela	ES	lmu	TT	-1.1	41.59	79	649	12-20	4.2-7.2	10.2-15.2
	Lutjewad	NL	lut	G	6.35	53.4	60	61	12-20	4.2-7.2	10.2-15.2
	Mace Head	IR	mhd	G	-9.9	53.33	15	40	12-20	4.2-7.2	10.2-15.2
	Ochsenkopf	DE	oxk	TT	11.81	50.03	163	1185	00-06	3.6	3.6
	Pallas	FI	pal	G	24.12	67.97	5	565	12-20	4.2-7.2	10.2-15.2
	Plateau Rosa	IT	prs	G	7.7	45.93	gl	3480	00-06	3.6	3.6
	Puy de Dôme	FR	puy	G	2.97	45.77	10	1475	00-06	3.6	3.6
	Schauinsland	DE	sch	G	7.92	47.9	gl	1205	00-06	3.6	3.6
	Trainou	FR	trn	TT	2.11	47.96	180	311	12-20	4.2-7.2	10.2-15.2
	Westerland	DE	wes	G	8.32	54.93	gl	12	12-20	4.2-7.2	10.2-15.2
ICOS50	Angus	UK	tta	TT	-2.98	56.56	220	520	12-20	4.2-7.2	10.2-15.2
	Egham	UK	egh	G	-0.55	51.43	5	45	12-20	4.2-7.2	10.2-15.2
	Norunda	SE	nor	TT	17.48	60.09	102	147	12-20	4.2-7.2	10.2-15.2
	Kresin u Pacova	CZ	kre	TT	15.08	49.57	250	790	12-20	4.2-7.2	10.2-15.2
	Hohenpeißenberg	DE	hpb	TT	11.01	47.8	159	1106	00-06	3.6	3.6
	Zugspitze	DE	zug	G	10.98	47.42	10	2660	00-06	3.6	3.6
	Risø Meteorological Mast	DK	ris	TT	12.09	55.65	125	130	12-20	4.2-7.2	10.2-15.2
	Høvsøre Wind Test Station	DK	hov	TT	8.15	56.44	116	116	12-20	4.2-7.2	10.2-15.2
	Carnsore Point EMEP monitoring Station	IR	crn	G	-6.33	52.06	3	3	12-20	4.2-7.2	10.2-15.2
	Malin Head Synoptic Meteorological Station	IR	mld	G	-7.37	55.38	3	13	12-20	4.2-7.2	10.2-15.2
	Katowice Kosztowy	PL	kat	TT	19.12	50.19	355	655	12-20	4.2-7.2	10.2-15.2

	Piła Rusionow	PL	pil	TT	16.26	53.17	320	455	12-20	4.2-7.2	10.2-15.2
	Jemiolow	PL	jem	TT	15.28	52.35	314	475	12-20	4.2-7.2	10.2-15.2
	Hyltemossa	SE	hyl	TT	13.42	56.1	150	255	12-20	4.2-7.2	10.2-15.2
	Observatoire Pérenne de l'Environnement	FR	ope	TT	5.36	48.48	120	512	12-20	4.2-7.2	10.2-15.2
	Observatoire de Haute Provence	FR	ohp	TT	5.71	43.93	100	740	12-20	4.2-7.2	10.2-15.2
	Pic du Midi	FR	pdm	G	0.14	42.94	10	2887	00-06	3.6	3.6
	SMEAR II Hyytiälä	FI	hyy	TT	24.29	61.85	127	308	12-20	4.2-7.2	10.2-15.2
	Puijo-Koli	FI	pui	TT	27.65	62.9	176	406	12-20	4.2-7.2	10.2-15.2
	ICOS eastern Finland Utö - Baltic sea	FI	uto	G	21.38	59.78	60	68	12-20	4.2-7.2	10.2-15.2
	Finokalia	GR	fik	G	25.67	35.34	2	152	12-20	4.2-7.2	10.2-15.2
	Birkenes Observatory	NO	bir	G	8.25	58.38	gl	190	12-20	4.2-7.2	10.2-15.2
	Andøya Observatory	NO	and	G	16.01	69.27	gl	380	12-20	4.2-7.2	10.2-15.2
	Svartberget	SE	sva	TT	19.78	64.26	150	385	12-20	4.2-7.2	10.2-15.2
	Tacolneston (norfolk)	UK	tac	G	1.14	52.52	191	261	12-20	4.2-7.2	10.2-15.2
	Ridge Hill	UK	rhi	G	-2.54	52	152	356	12-20	4.2-7.2	10.2-15.2
	Delta Ebre	ES	dec	TT	0.79	40.74	11	16	12-20	4.2-7.2	10.2-15.2
	Valderejo	ES	val	TT	-3.21	42.87	25	1100	00-06	3.6	3.6
	Xures-Invernadeiro	ES	xic	TT	-8.02	41.98	30	902	12-20	4.2-7.2	10.2-15.2
	Ispra	IT	isp	G	8.63	45.81	40	230	12-20	4.2-7.2	10.2-15.2
ICOS66	Lindenberg	DE	lin	TT	14.12	52.21	99	192	12-20	4.2-7.2	10.2-15.2
	Mannheim	DE	man	TT	8.49	49.49	213	323	12-20	4.2-7.2	10.2-15.2
	Gartow 2	DE	grt	TT	11.44	53.07	344	410	12-20	4.2-7.2	10.2-15.2
	Messkirch/Rohrdorf	DE	msr	TT	9.12	48.02	240	892	12-20	4.2-7.2	10.2-15.2
	Wesel	DE	wsl	TT	6.57	51.65	321	340	12-20	4.2-7.2	10.2-15.2
	Helgoland	DE	hlg	G	7.9	54.18	10	40	12-20	4.2-7.2	10.2-15.2
	Iznajar	ES	izn	TT	-4.38	37.28	5	555	12-20	4.2-7.2	10.2-15.2
	Hengelo	NL	hen	G	6.75	52.34	70	80	12-20	4.2-7.2	10.2-15.2
	Goes	NL	goe	G	3.78	51.48	70	70	12-20	4.2-7.2	10.2-15.2
	Peel	NL	pee	G	5.98	51.37	70	80	12-20	4.2-7.2	10.2-15.2
	Noordzee	NL	nse	G	4.73	54.85	50	50	12-20	4.2-7.2	10.2-15.2
	Cap Corse	FR	cor	G	9.35	42.93	35	85	12-20	4.2-7.2	10.2-15.2
	Roc Tredudon	FR	roc	G	-3.91	48.41	10	373	12-20	4.2-7.2	10.2-15.2
	Alfabia	ES	alf	TT	2.72	39.74	gl	1069	00-06	3.6	3.6
	Saissac	FR	sai	TT	2.1	43.39	300	800	00-06	3.6	3.6
	NIO	FR	nio	TT	0.05	46.19	330	503	12-20	4.2-7.2	10.2-15.2

1124

1125

1126

1127 **Table A2.** NEE uncertainty budget for European countries for July 2007 estimated using the
1128 reference inversion configuration and different atmospheric CO₂ networks. Uncertainty
1129 reduction values (UR) are shown in the last two columns.

Country	NEE, TgCcountry ⁻¹ month ⁻¹	NEE prior unc. TgCcountry ⁻¹ month ⁻¹	NEE post. Unc.		UR (%)	
			TgCcountry ⁻¹ month ⁻¹		ICOS23	ICOS66
			ICOS23	ICOS66		
Austria	-3.95	4.60	1.49	1.56	68	66
Belgium	-1.05	1.88	0.69	0.69	63	63
Bulgaria	-1.22	5.72	5.43	4.06	5	29
Croatia	-1.64	2.27	1.17	1.13	48	50
Cyprus	0.04	0.18	0.18	0.18	0	1
Czech Republic	-4.35	4.08	2.06	1.52	50	63
Denmark	-1.97	1.74	1.35	0.76	22	57
Estonia	-2.67	2.37	1.66	1.42	30	40
Finland	-8.37	11.56	5.92	3.14	49	73
France	-17.16	18.41	3.52	3.04	81	84
Germany	-16.00	14.20	4.73	2.73	67	81
Greece	0.09	3.58	3.45	2.89	4	19
Hungary	-2.19	4.95	2.61	2.31	47	53
Ireland	-2.49	2.42	1.68	1.27	30	48
Italy	-4.44	9.83	4.24	3.82	57	61
Latvia	-3.61	3.32	2.33	2.22	30	33
Lithuania	-3.92	3.42	2.02	2.10	41	39
Luxembourg	-0.12	0.17	0.10	0.10	42	44
Netherlands	-0.97	1.99	0.65	0.50	68	75
Norway	-6.02	9.65	4.85	4.65	50	52
Poland	-21.10	13.26	5.02	4.24	62	68

Portugal	-1.17	4.24	3.71	2.80	12	34
Romania	-7.14	10.79	9.14	8.34	15	23
Slovakia	-2.82	2.59	1.30	1.30	50	50
Slovenia	-1.17	1.04	0.48	0.43	54	58
Spain	-3.54	19.90	7.16	3.97	64	80
Sweden	-9.84	16.50	7.53	5.62	54	66
Switzerland	-1.72	2.61	1.03	0.68	60	74
UK	-8.52	7.56	2.11	1.59	72	79

1130

1131

1132

1133

1134

1135

1136

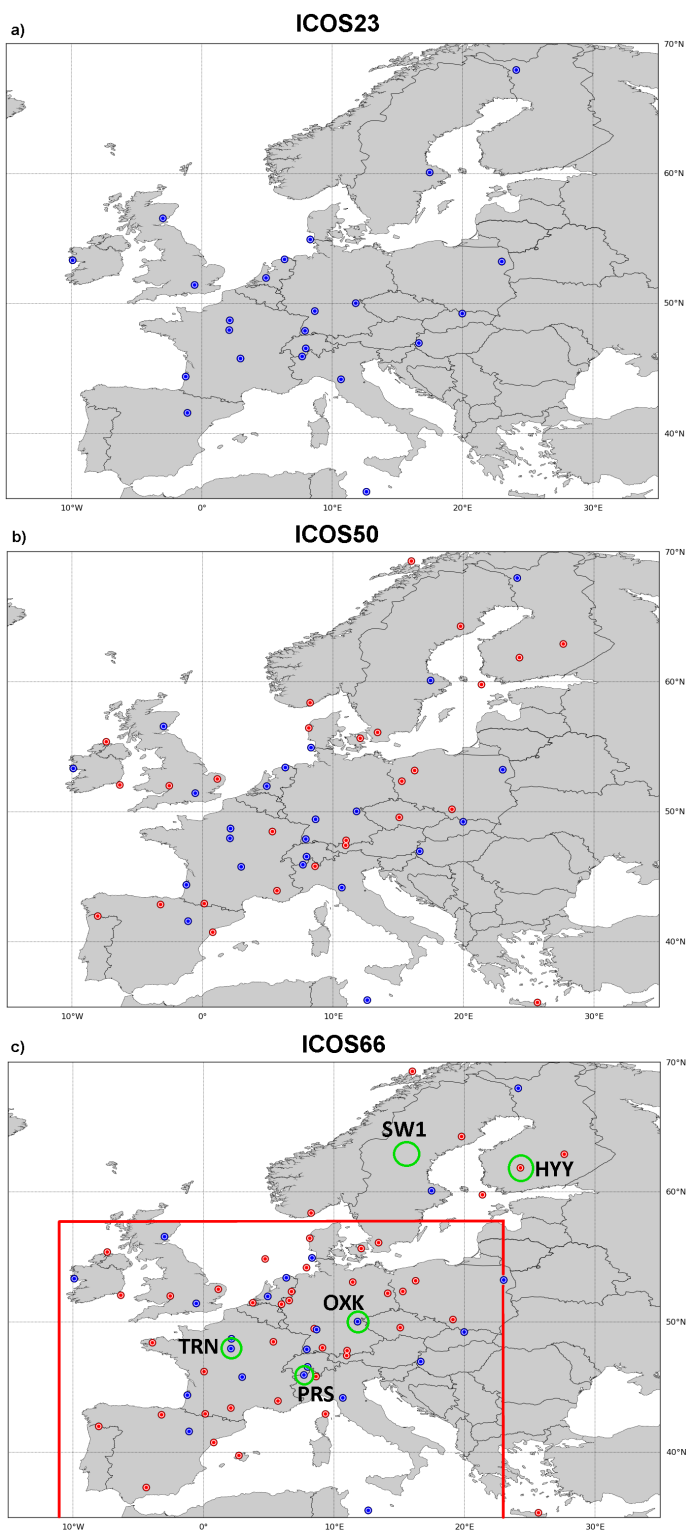


Figure 1. Site location for the different ICOS network configurations used in this study: (a) ICOS23 (b) ICOS50 (c) ICOS66. Dark blue circles correspond to ICOS23 and the red circles are the new sites for ICOS50 and ICOS66 compared to ICOS23. The European domain ($\sim 6.8 \times 10^6$ km² of land surface) covered by these figures corresponds to the domain of the configuration of the CHIMERE atmospheric transport model used in this study. The red rectangle in (c)

corresponds to a western European domain (WE domain, $\sim 3.5 * 10^6$ km² of land surface) which is used for some of the present analysis because it is significantly better sampled by the ICOS networks than other areas. Green circles in (c) are the station locations used for the study of the uncertainty reduction as a function of the spatial scale of the aggregation around each station (in Sect. 3.1.4).

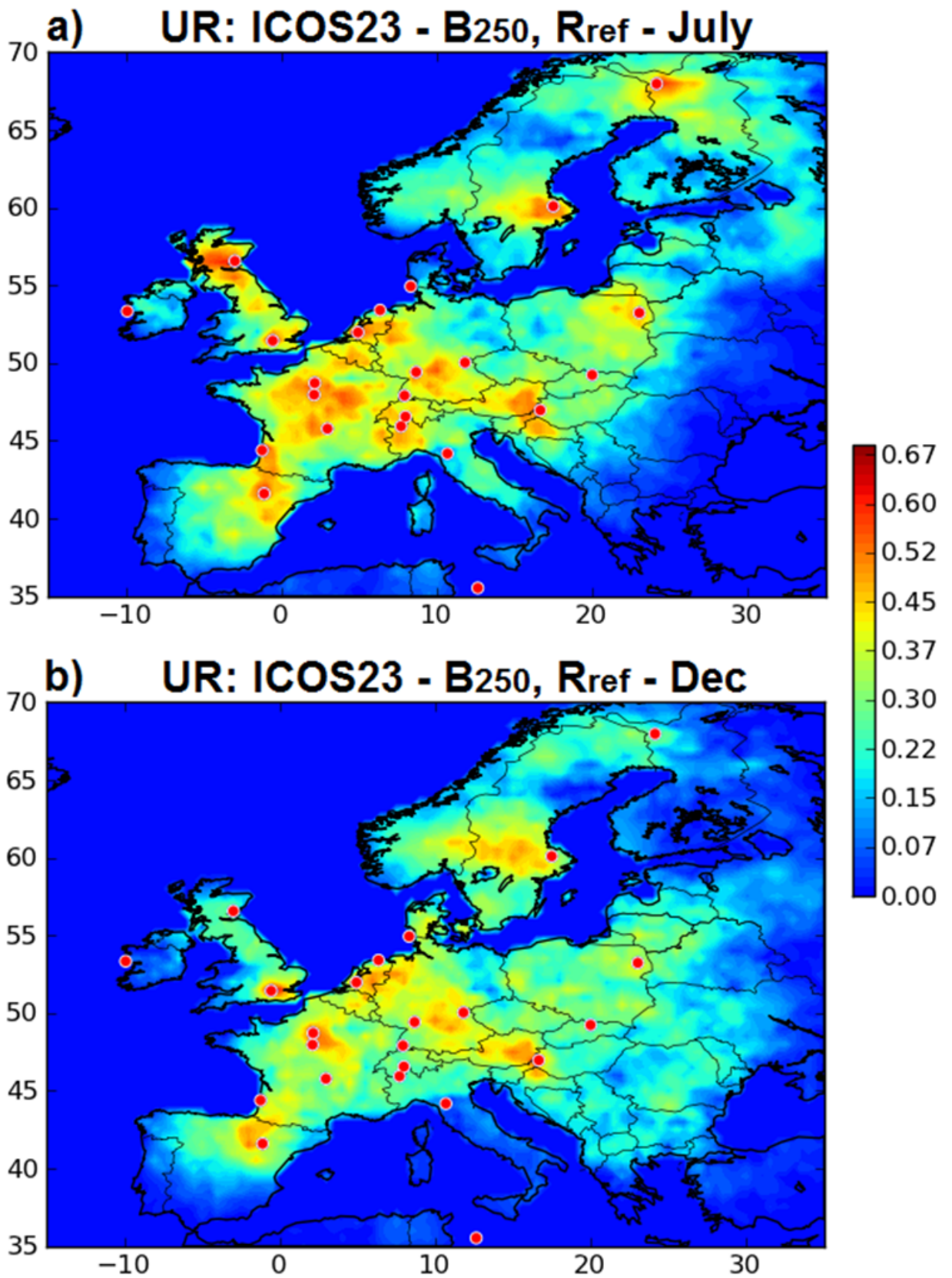


Figure 2. Uncertainty reduction (theoretically comprised between 0 and 1) for two-week mean NEE at 0.5° resolution in July (a) and in December (b) when using ICOS23 (red dots) and the

1166 reference inversion setup. Red/blue colors indicate relatively high/low uncertainty reduction
1167 (with min = 0, max = 0.68 in the color scale).

1168

1169

1170

1171

1172

1173

1174

1175

1176

1177

1178

1179

1180

1181

1182

1183

1184

1185

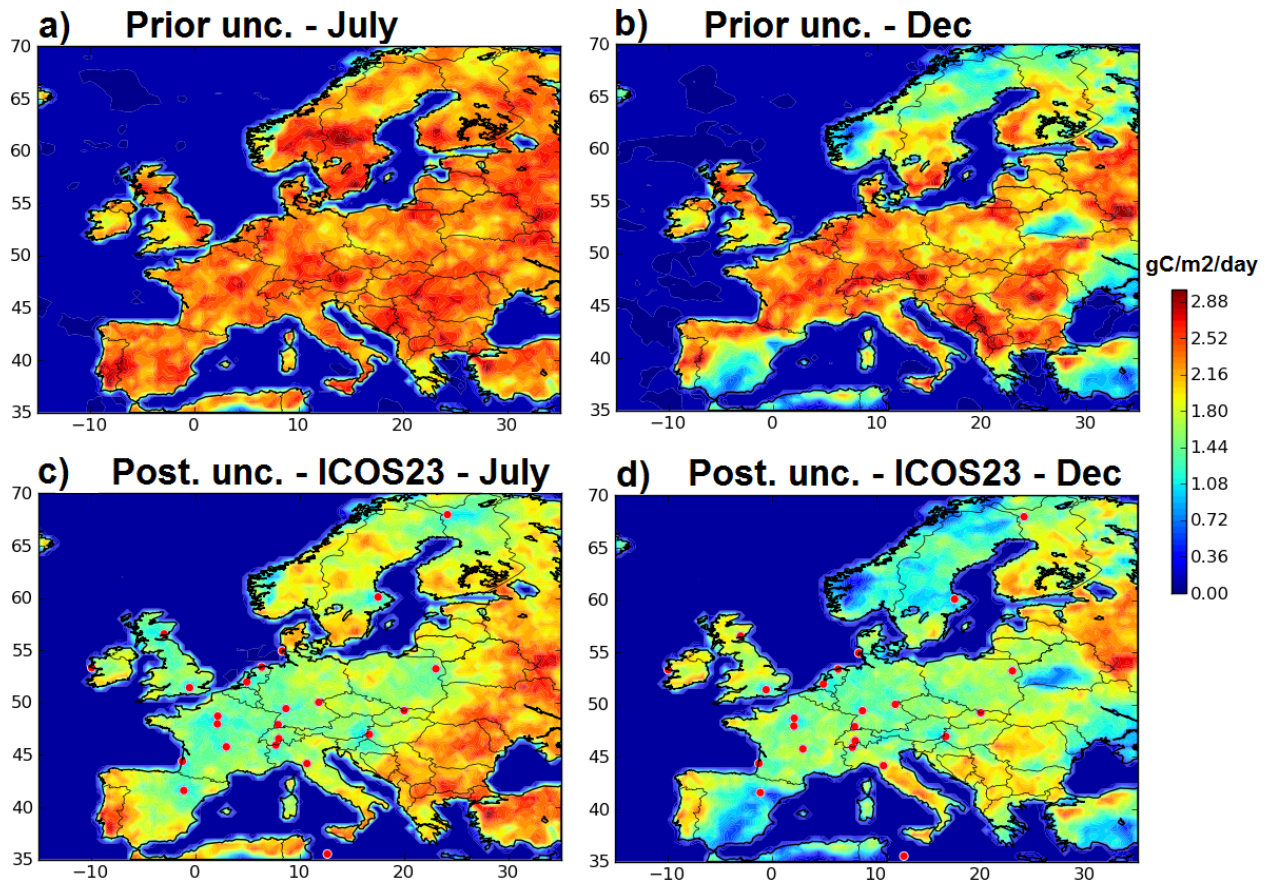


Figure 3. Standard deviations ($\text{gCm}^{-2}\text{day}^{-1}$) of the prior (a,b) and posterior (c,d) uncertainties in two-week mean NEE at 0.5° resolution for (a,c) July and (b,d) December. Posterior uncertainties are given for inversions using ICOS23 (red dots) and the reference inversion setup. Red/blue colors indicate relatively high/low uncertainties (with $\text{min} = 0 \text{ gCm}^{-2}\text{day}^{-1}$, $\text{max} = 3 \text{ gCm}^{-2}\text{day}^{-1}$ in the color scale).

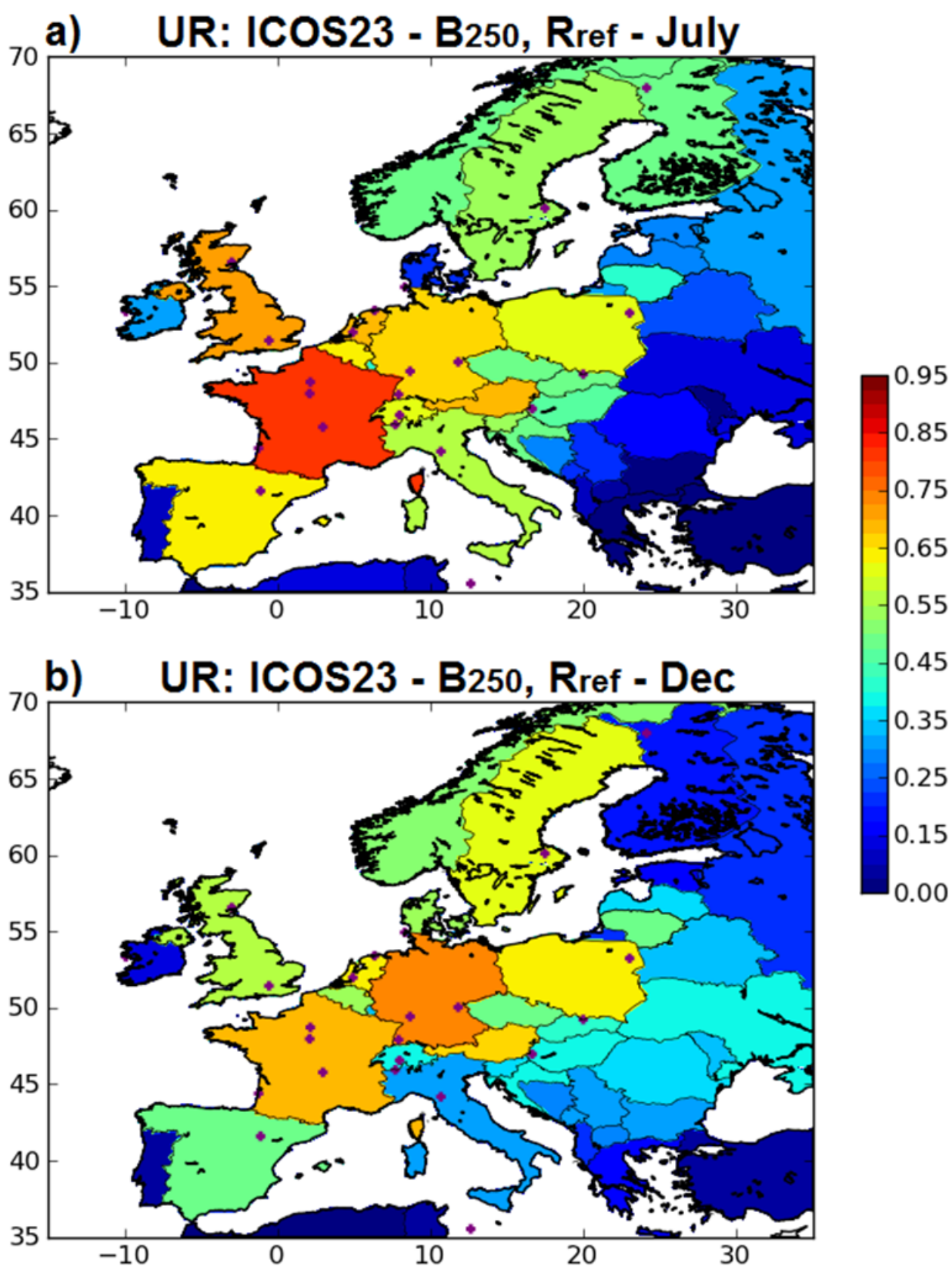


Figure 4. Uncertainty reduction (theoretically comprised between 0 and 1) for two-week mean NEE at the country scale for July (a) and December (b) when using ICOS23 and the reference

1201 inversion configuration. Red/blue colors indicate relatively high/low uncertainty reduction (with
1202 min = 0, max = 0.95 in the color scale).

1203

1204

1205

1206

1207

1208

1209

1210

1211

1212

1213

1214

1215

1216

1217

1218

1219

1220

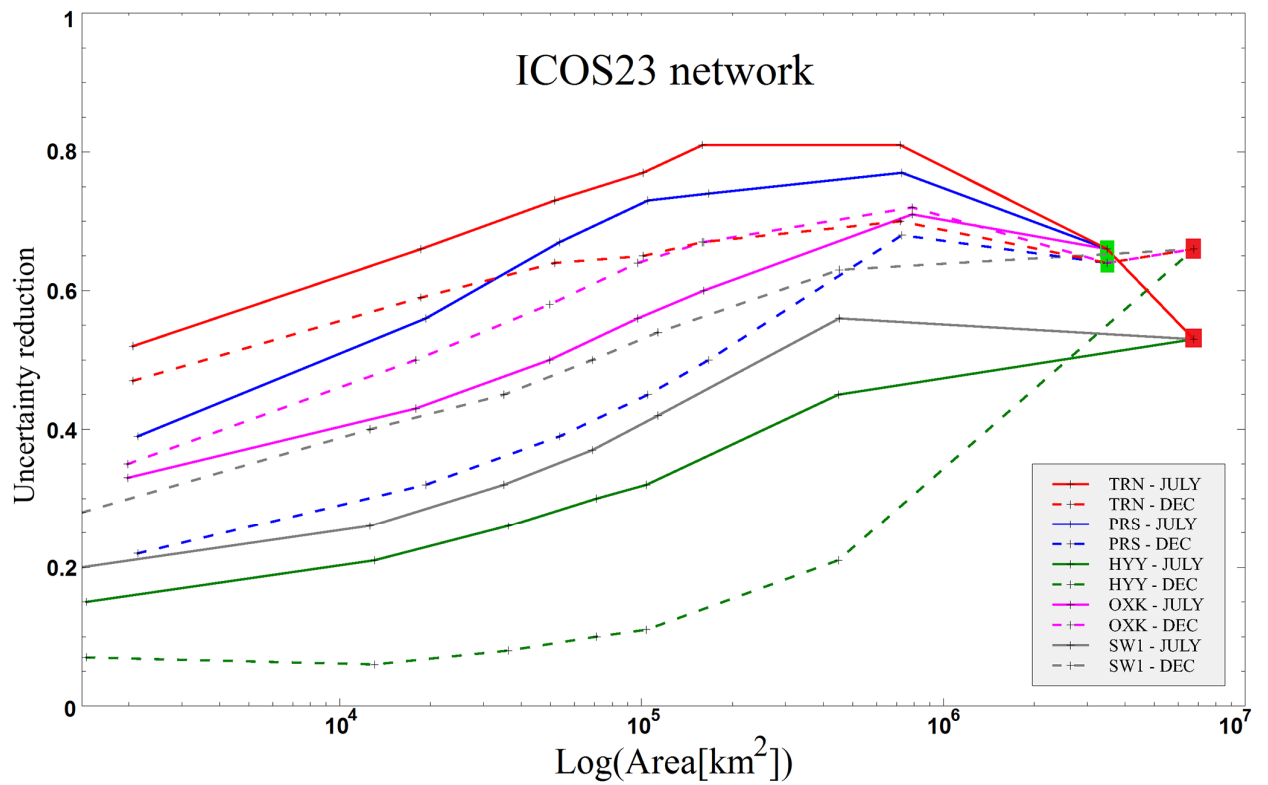


Figure 5. Uncertainty reduction (theoretically comprised between 0 and 1) for two-week mean NEE in July and December 2007 using ICOS23 and the reference configuration of the inversion, as a function of the size (logarithmic scale) of the spatial averaging area (in km^2 ; for each curve values are derived for $1.5^\circ \times 1.5^\circ$, $2.5^\circ \times 2.5^\circ$, $3.5^\circ \times 3.5^\circ$, $4.5^\circ \times 4.5^\circ$ and $10.5^\circ \times 10.5^\circ$ areas which correspond to different values in terms of km^2 depending on their location in Europe) around each station TRN (red curves), PRS (blue curves), HYY (green curves), OXK (pink curves) and SW1 (grey curves; see the locations in Fig. 1c). Solid and dash lines correspond to results for July and December respectively (see the legend within the figure). The results of uncertainty reduction for the whole European domain are included (red rectangle). The results for the western European domain defined in Fig. 1c are included on curves corresponding to sites which are located in this domain (TRN, PRS and OXK, see the green rectangle).

Posterior error correlations

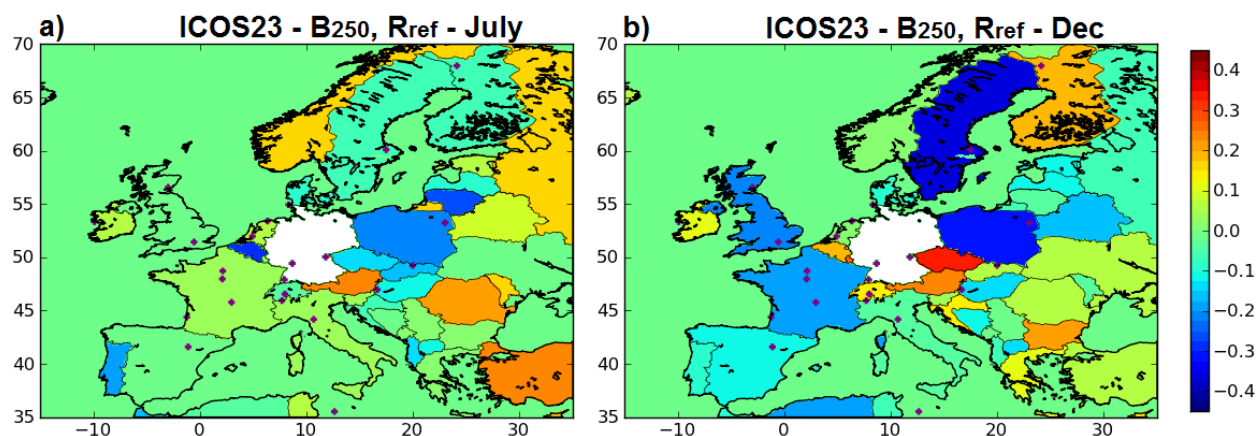


Figure 6. Correlations of the posterior uncertainties in two-week mean NEE between Germany and the other European countries in July **(a)** and December **(b)** from the reference inversions with ICOS23. Germany is masked in white. Red/blue colors indicate relatively high positive/negative correlations (with min= -0.45, max = 0.45 in the color scale).

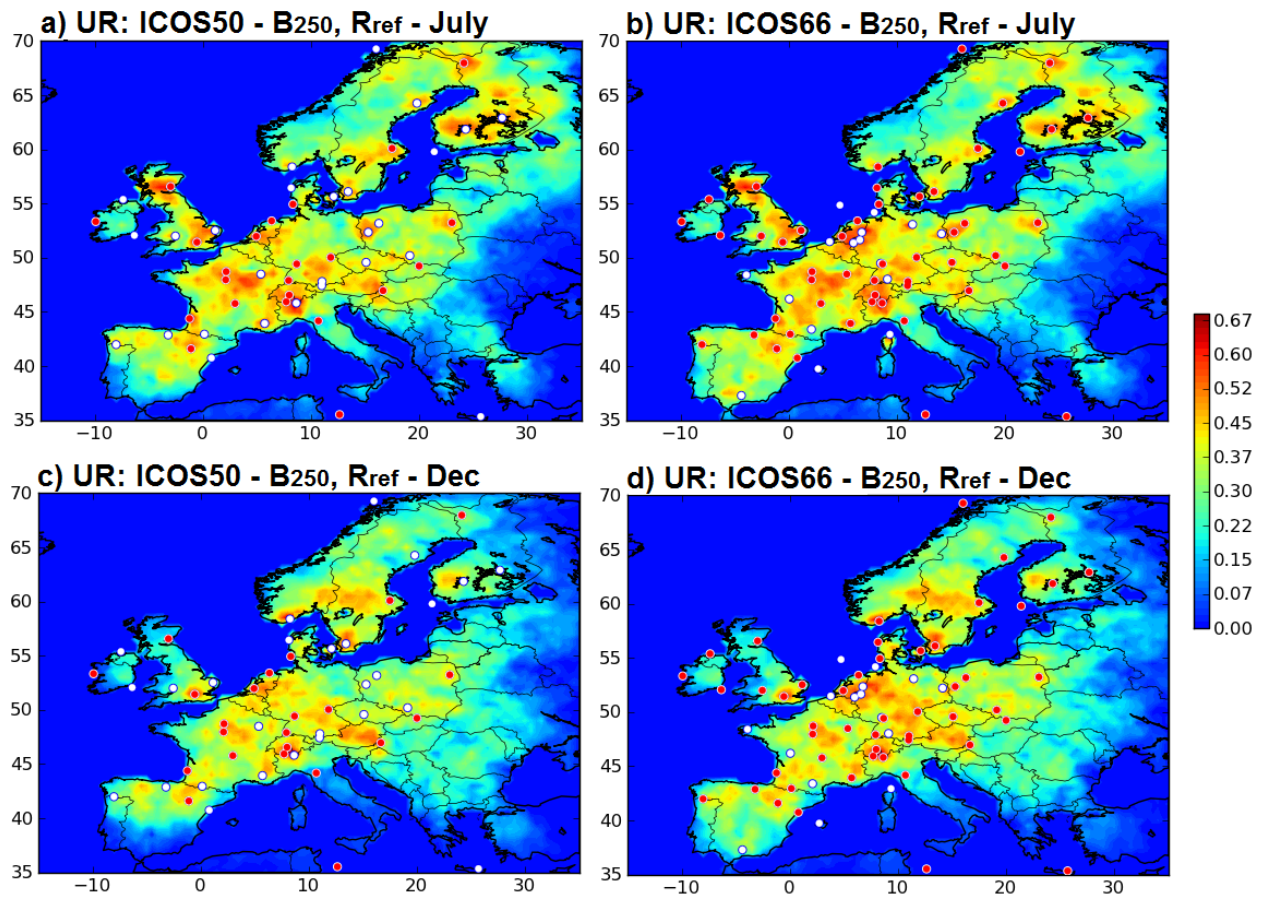


Figure 7. Uncertainty reduction (theoretically comprised between 0 and 1) for two-week mean NEE at 0.5° resolution in July (a,b) and December (c,d) when using ICOS50 (a,c) and ICOS66 (b,d) and the reference inversion configuration. Red dots corresponds to the ICOS23 (a,c) or ICOS50 (b,d) sites while white dots correspond to the additional sites included in ICOS50 or ICOS66 respectively. Red/blue colors indicate relatively high/low uncertainty reduction (with min = 0, max = 0.68 in the color scale).

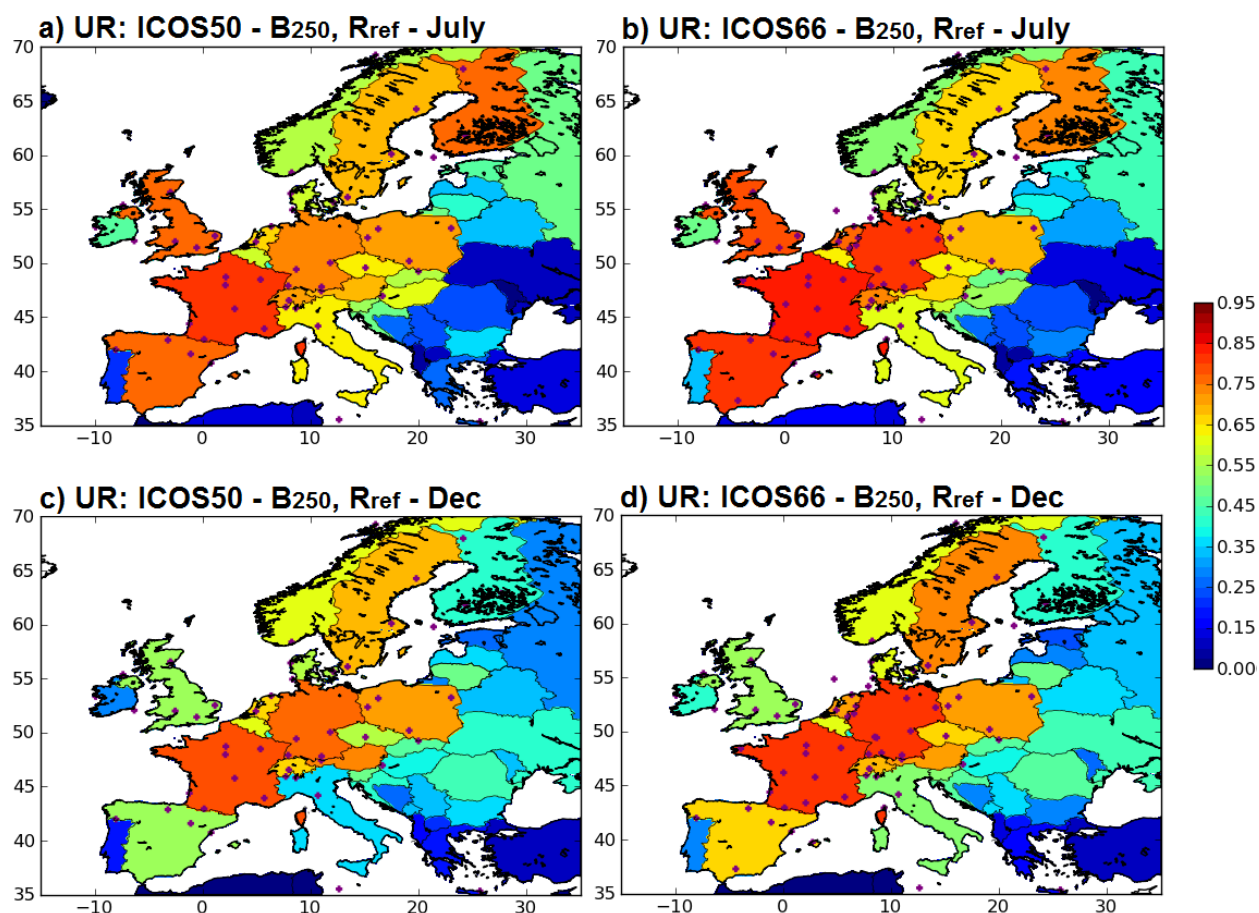


Figure 8. Uncertainty reduction (theoretically comprised between 0 and 1) for two-week mean NEE at the country scale in July (a,b) and December (c,d), when using ICOS50 (a,c) and ICOS66 (b,d). Red/blue colors indicate relatively high/low uncertainty reduction (with min = 0, max = 0.95 in the color scale).

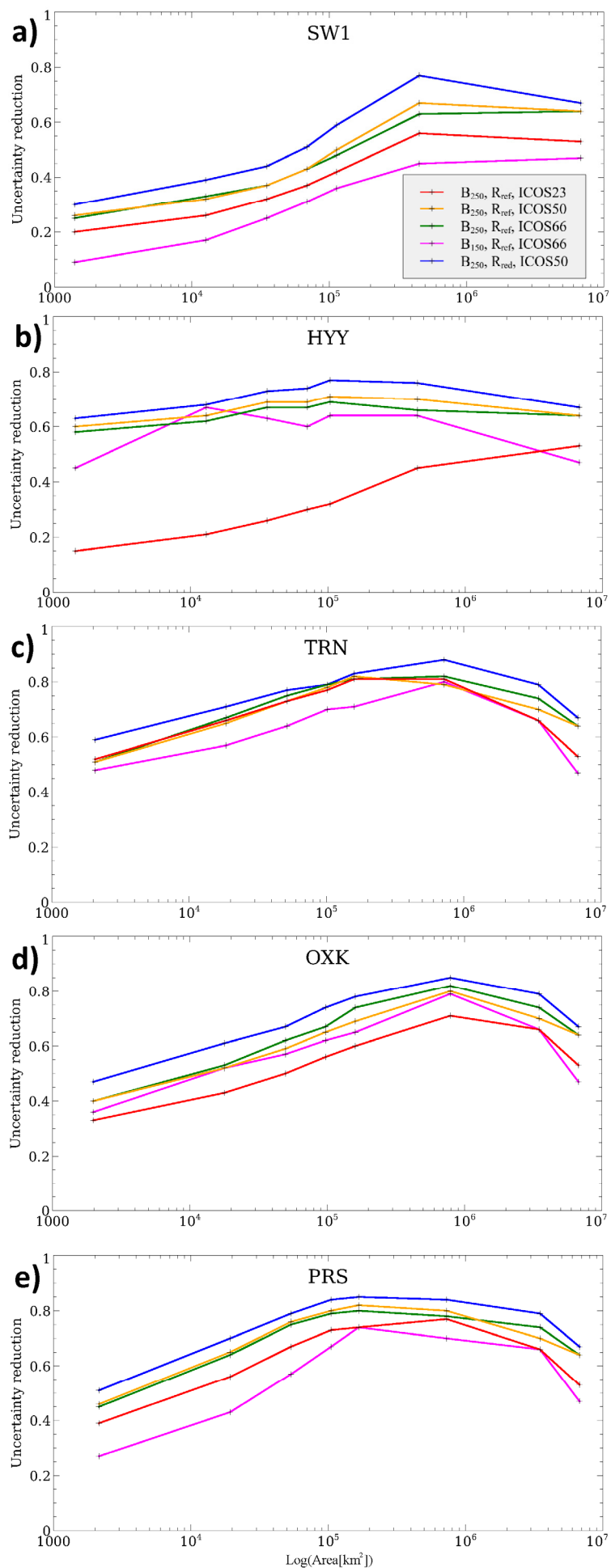


Figure 9. Uncertainty reduction (theoretically comprised between 0 and 1) for two-week mean NEE for July 2007 as a function of the size (in logarithmic scale) of the spatial averaging area centered on **(a)** SW1, **(b)** HYY, **(c)** TRN, **(d)** OXK, and **(e)** PRS. Red, orange, green lines: results with the reference configuration of the inversion using ICOS23, ICOS50 and ICOS66 respectively; blue: results when using ICOS50 and the inversion configuration with $\mathbf{R}=\mathbf{R}_{\text{red}}$; pink: results when using ICOS66 and the inversion configuration with $\mathbf{B}=\mathbf{B}_{150}$. The results of uncertainty reduction for the whole European domain are included systematically. The results for the western European domain defined in Fig. 1c are included on curves corresponding to sites which are located in this domain (TRN, PRS and OXK).

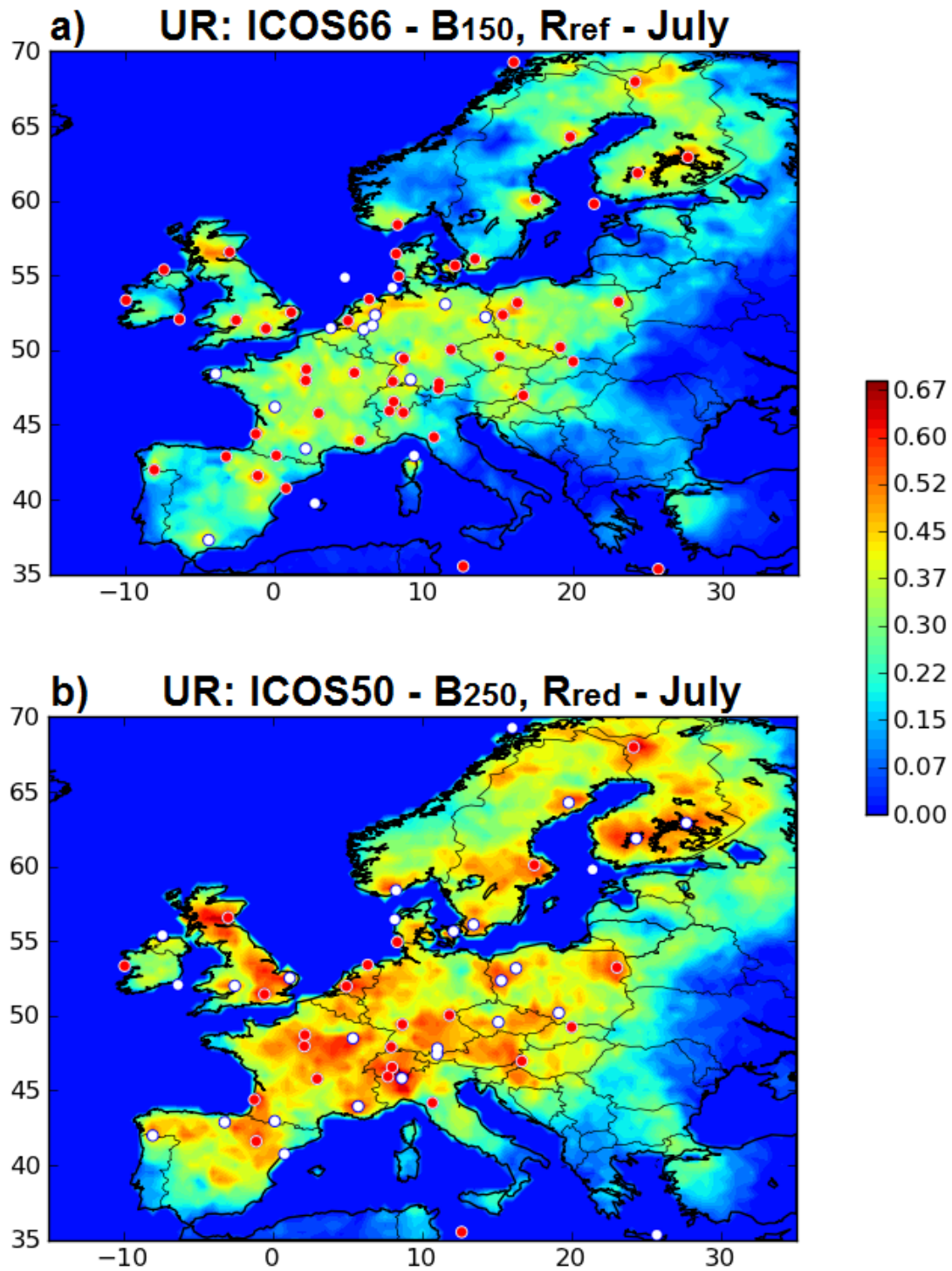


Figure 10. Uncertainty reduction (theoretically comprised between 0 and 1) for two-week mean NEE at 0.5° horizontal resolution in July when modifying the inversion configuration from the reference one: using \mathbf{B}_{150} instead of \mathbf{B}_{250} and ICOS66 (a) using \mathbf{R}_{red} instead of \mathbf{R}_{ref} and ICOS50 (b). Red dots corresponds to the ICOS23 (b) or ICOS50 (a) sites while white dots correspond to the additional sites included in ICOS50 or ICOS66 respectively. Red/blue colors indicate relatively high/low uncertainty reduction (with min = 0, max = 0.68 in the color scale).

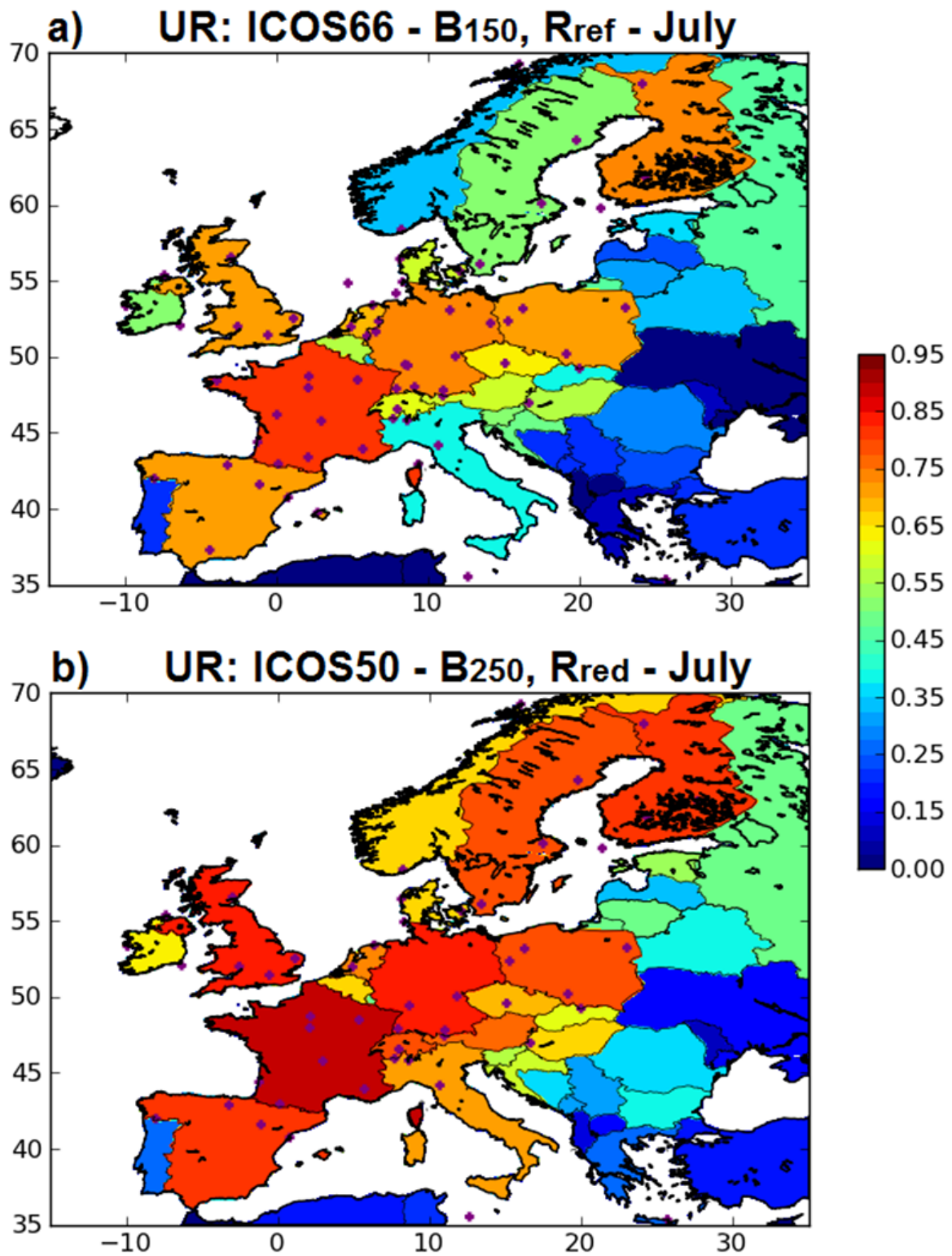


Figure 11. Uncertainty reduction (theoretically comprised between 0 and 1) for two-week mean NEE at the country scale in July when modifying the inversion configuration from the reference one by using \mathbf{B}_{150} instead of \mathbf{B}_{250} and ICOS66 (a) using \mathbf{R}_{red} instead of \mathbf{R}_{ref} and ICOS50 (b). Red/blue colors indicate relatively high/low uncertainty reduction (with min = 0, max = 0.95 in the color scale).

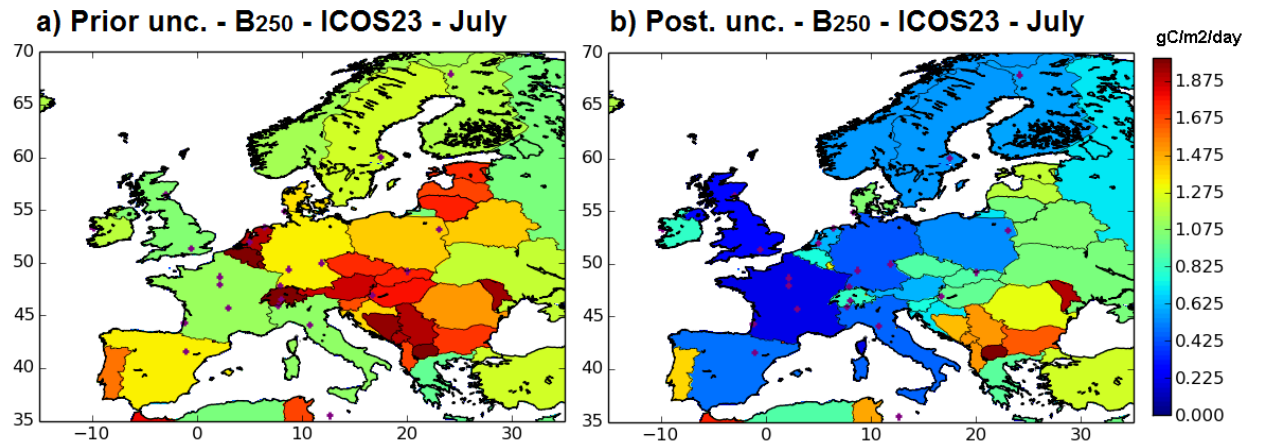


Figure 12. Standard deviations ($\text{gCm}^{-2}\text{day}^{-1}$) of the prior (a) and posterior (b) flux uncertainties at country scale. Posterior uncertainties are given for inversions using ICOS23 (red dots) and the reference inversion setup. Red/blue colors indicate relatively high/low uncertainties (with min = 0 $\text{gCm}^{-2}\text{day}^{-1}$, max = 1.975 $\text{gCm}^{-2}\text{day}^{-1}$ in the color scale).

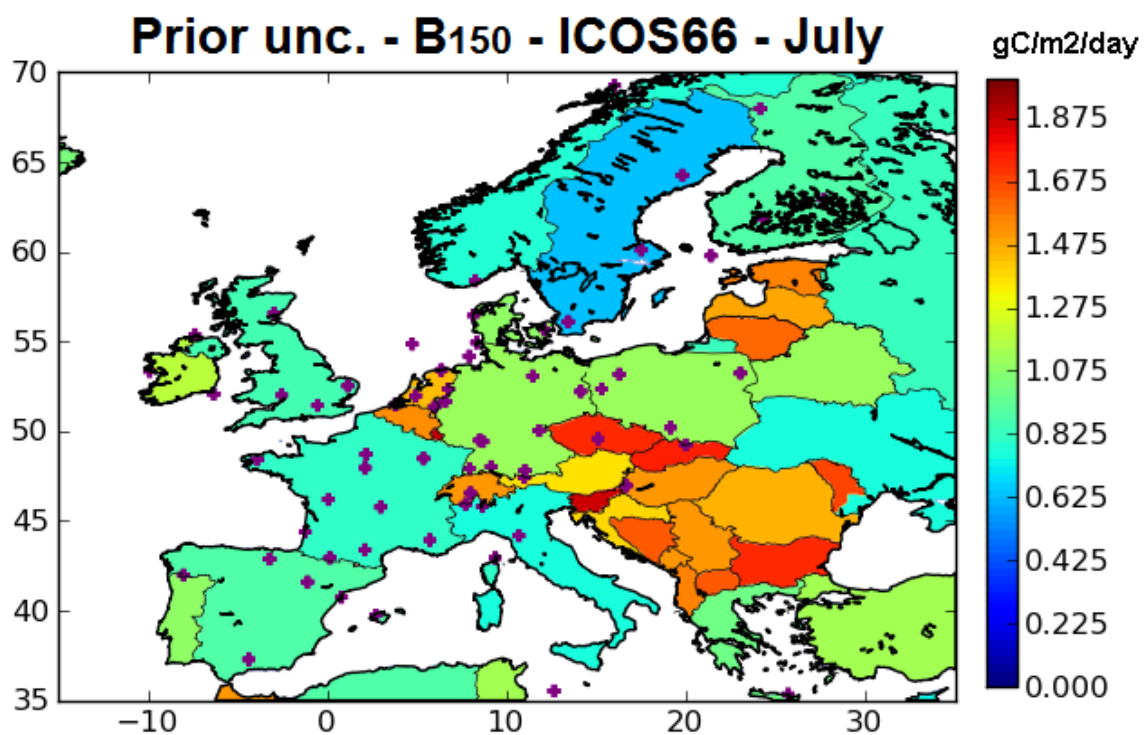


Figure A1. Standard deviations ($\text{gCm}^{-2}\text{day}^{-1}$) of the prior flux uncertainties at country scale for July when considering \mathbf{B}_{150} . Red dots: ICOS66. Red/blue colors indicate relatively high/low uncertainties (with $\text{min} = 0 \text{ gCm}^{-2}\text{day}^{-1}$, $\text{max} = 1.975 \text{ gCm}^{-2}\text{day}^{-1}$ in the color scale).

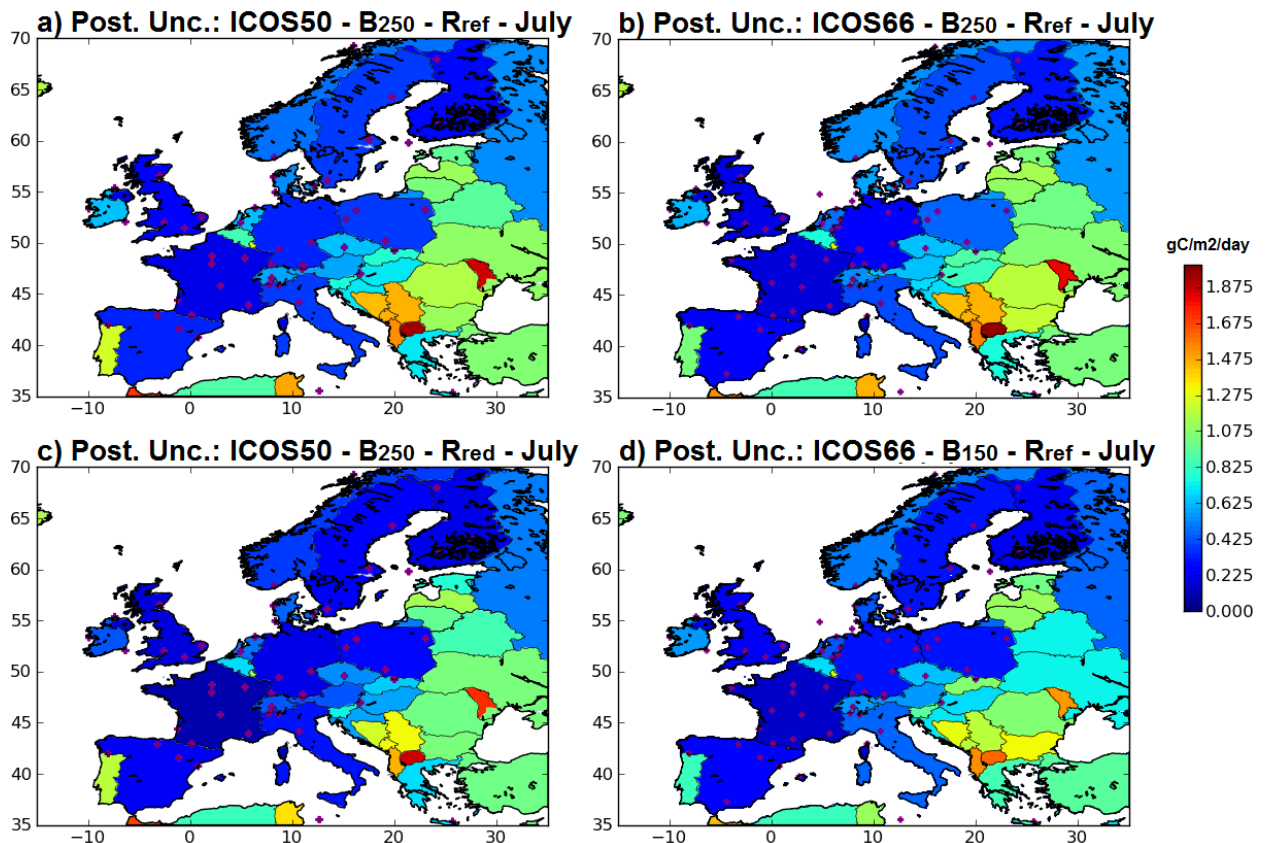


Figure A2. Standard deviations ($\text{gCm}^{-2}\text{day}^{-1}$) of the posterior uncertainties at country scale for July when using ICOS50 (a,c) and ICOS66 (b,d), the reference inversion configuration (a,b), using \mathbf{B}_{150} instead of \mathbf{B}_{250} (d) using \mathbf{R}_{red} instead of \mathbf{R}_{ref} (c). Red/blue colors indicate relatively high/low uncertainties (with min = 0 $\text{gCm}^{-2}\text{day}^{-1}$, max = 1.975 $\text{gCm}^{-2}\text{day}^{-1}$ in the color scale).

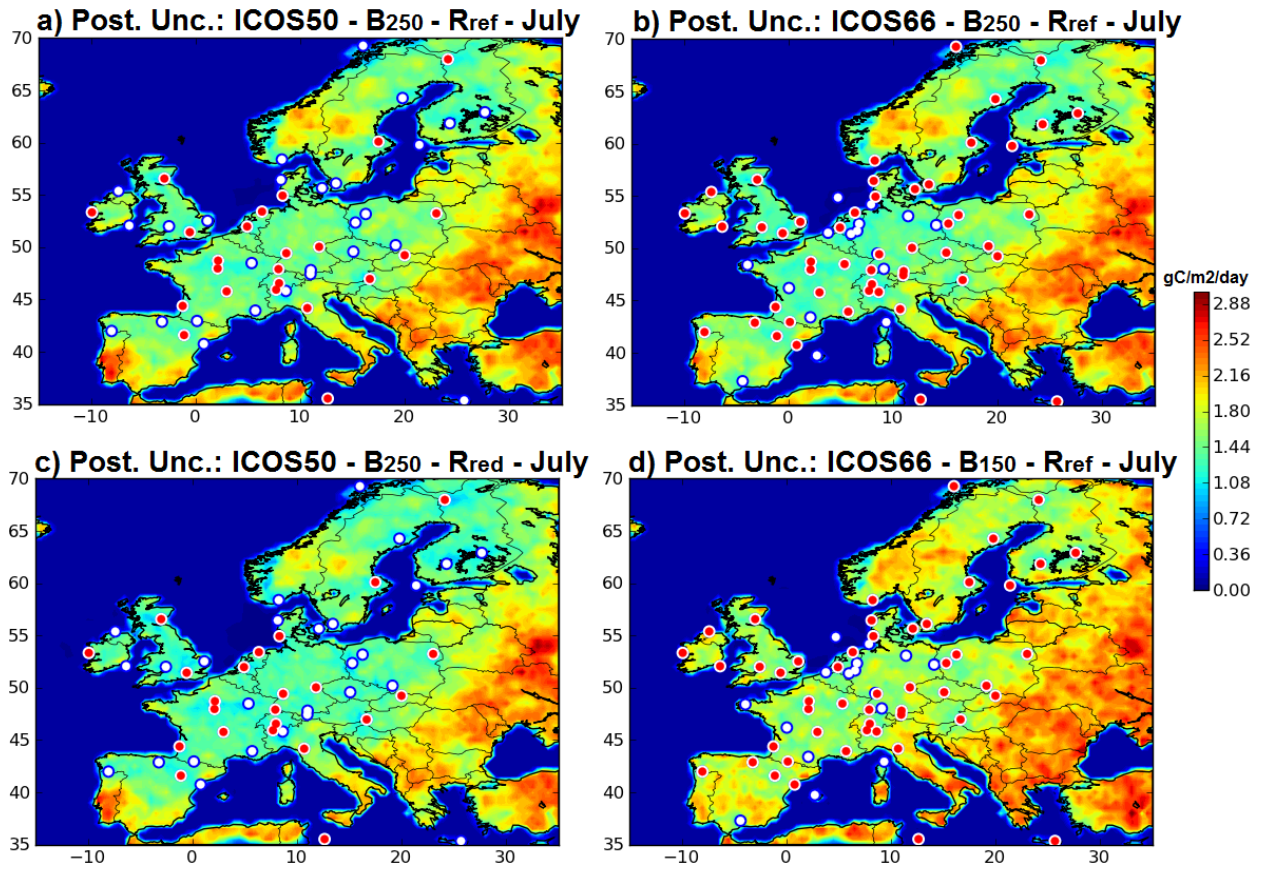


Figure A3. Standard deviations ($\text{gCm}^{-2}\text{day}^{-1}$) of the posterior uncertainties in two-week mean NEE at 0.5° resolution for July when using ICOS50 (a,c) and ICOS66 (b,d), the reference inversion configuration (a,b), using \mathbf{B}_{150} instead of \mathbf{B}_{250} (d) using \mathbf{R}_{red} instead of \mathbf{R}_{ref} (c). Red dots corresponds to the ICOS23 (a,c) or ICOS50 (b,d) sites while white dots correspond to the additional sites included in ICOS50 or ICOS66 respectively. Red/blue colors indicate relatively high/low uncertainties (with $\text{min} = 0 \text{ gCm}^{-2}\text{day}^{-1}$, $\text{max} = 3 \text{ gCm}^{-2}\text{day}^{-1}$ in the color scale).